Article

(E)-2-Benzylidenecyclanones: Part XX. Reaction of Cyclic Chalcone Analogs with Cellular Thiols. Unexpected Increased Reactivity of 4-Chromanone- Compared to 1-Tetralone-Analogs in Thia-Michael Reactions [1]

Gábor Bognár , Fatemeh Kenari , Zoltán Pintér , Igor D Borges , Ademir J Camargo , Heibbe C. B. De Oliveira , Flávio O Sanches-Neto , Valter H Carvalho-Silva , Hamilton B Napolitano , Pál Perjési *

Posted Date: 17 July 2024

doi: 10.20944/preprints202407.1444.v1

Keywords: chalcone; homoisoflavones; benzylidenechromanones; anticancer activity; glutathione; N-acetylcysteine; thia-Michael addition; Molecular electrostatic; DFT calculations

Article

(*E*)-2-Benzylidenecyclanones: Part XX: Reaction of Cyclic Chalcone Analogs with Cellular Thiols: Unexpected Increased Reactivity of 4-Chromanone- Compared to 1-Tetralone-Analogs in thia-Michael Reactions [1]

Gábor Bognár [1], Fatemeh Kenari [1], Zoltán Pintér [1], Igor D. Borges [2], Ademir J. Camargo [2], Heibbe C. B. Oliveira [3], Flávio Olimpio Sanches-Neto [3,4], Valter H. Carvalho-Silva [5], Hamilton B. Napolitano [2] and Pál Perjési [1,2,*]

[1] Institute of Pharmaceutical Chemistry, University of Pécs, H-7624, Pécs, Hungary
[2] Grupo de Química Teórica e Estrutural de Anápolis, Universidade Estadual de Goiás, Anápolis, GO, Brazil
[3] Laboratório de Estrutura Eletrônica e Dinâmica Molecular, Universidade Federal de Goiás, Goiânia, GO, Brazil
[4] Instituto Federal de Educação, Ciência e Tecnologia de Goiás, 72876-601, Valparaíso de Goiás, GO, Brazil; Instituto de Química, Universidade de Brasília, Caixa Postal 4478, 70904-970, Brasília, Brazil
[5] Laboratory for Modeling of Physical and Chemical Transformations, Research and Graduate Center, Goiás State University, 75132-903, Anápolis, Brazil
* Correspondence: pal.perjesi@gytk.pte.hu; Tel.: +36-72-503-650

Abstract: *In vitro* cancer cell cytotoxicity (IC_{50} values) of (*E*)-3-(4′-methylbenzylidene)-4-chromanone (**IIIb**) showed >50.0 decreases in comparison to those of the respective tetralone derivative (**IIIc**). On the other hand, such a decrease was not observed in the analogous 4-OCH_3 (**IIc** and **IIIc**) derivatives. Since the compounds can be considered cyclic chalcone analogs, kinetics and diastereoselectivity of non-enzyme catalyzed reactions with reduced glutathione (GSH) and N-acetylcysteine (NAC) of **IIIb** and **IIIc** were investigated to assess the possible role of thiol-reactivity in the increased cytotoxicity of **IIIb**. Reactivity of the compounds and stereochemical outcome of the reactions were evaluated using high-pressure liquid chromatography-mass spectrometry (HPLC-MS). Molecular modeling calculations were performed to rationalize the observed differences in the thiol-reactivities of the chromanones (**III**) and the previously investigated tetralones (**II**). The results indicated possible role of spontaneous thiol-reactivity of compounds **III** in their recorded biological effects.

Keywords: chalcone; homoisoflavones; benzylidenechromanones; anticancer activity; glutathione; N-acetylcysteine; thia-Michael addition; Molecular electrostatic; DFT calculations

1. Introduction

Chalcones (I) are natural compounds, most often found in higher plants, especially in members of the *Leguminosae*, *Asteraceae*, and *Moraceae* families [2]. These plants are often used in traditional medicine, so the anti-inflammatory, cytotoxic, antimicrobial, antifungal, antidiabetic, and chemopreventive effects of chalcones are extensively studied in several laboratories [2,3]. Recognizing the multifaceted biological effects of natural chalcones, which can also be used pharmacologically, the synthesis and biological effects of a large number of synthetic chalcones were investigated and are still ongoing. These results are summarized in several review papers [4-7].

Earlier, we reported on the synthesis, stereochemistry, and *in vitro* cancer cell cytotoxicity of chalcones (**I**) and cyclic chalcone analogs (**II, III, IV**) against human Molt 4/8 and CEM T-lymphocytes as well as murine L1210 cells [8-10]. Among them, (*E*)-2-(X-benzylidene)-1-benzosuberones (**IV**) and (*E*)-3-(X-benzylidene)-4-chromanones (**III**) were the most prosperous class of compounds.

Comparison of the IC_{50} values of the investigated chromanone (**III**) derivatives with those of the carbocyclic analogs (**II**) with the same ary substituent showed the 4-CH_3 (**IIIb**) derivative outstanding potency in comparison with the respective **IIb** (the ratio of the IC_{50} values is >50.0). On the other hand, such an increase was not observed in the analogous 4-OCH_3 (**IIc** and **IIIc**) derivatives [10].

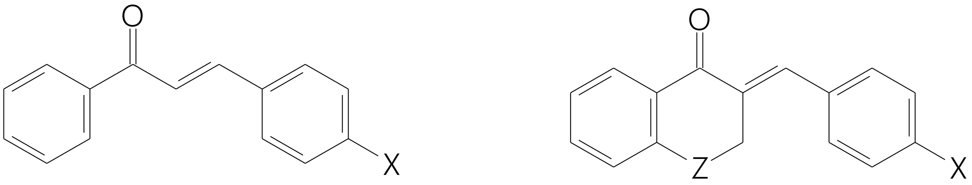

I

II Z= CH_2
III Z = O
IV Z = $(CH_2)_2$

X= H (a), CH_3 (b), OCH_3 (c)

Figure 1. Structure of 4-X-chalcones (**I**) and (*E*)-2-(4'-X-phenylmethylene)-1-tetralones (**II**), -bezosuberones (**IV**), and (*E*)-3-(4'-X-phenylmethylene)-4-chomanonones (**III**).

Several biological effects (e.g., NF-κB pathway inhibition (anti-inflammatory effect) [11,12], activation of the Nrf2 pathway (antitumor/cytoprotective effect) [12-14], inhibition of protein kinases (antitumor effect) [15,16], and interaction with tubulin at colchicine binding site (antimitotic effect) [15-18] of chalcones have been associated with their Michael-type reactivity toward cysteine residues of proteins. On the other hand, the dimensional shape of the molecules has also been reported as a determining factor in their biological activities [19].

The initial aim of the present study was to investigate the thiol reactivity of **IIIb** and **IIIc** and compare it with that of the previously investigated **IIb** and **IIc** [1]. Similar to our previous studies [1,20], reduced glutathione (GSH) and N-acetylcysteine (NAC) were used as thiol reagents. Reaction of thiols with chalcones (**I**) resulted in formation of the respective adducts. The soft nucleophilic thiols preferably react with the beta-carbon atom of the enone moiety, generating a chiral carbon atom [20]. In the reaction of the cyclic chalcone analogs (**II-IV**), the alfa-carbon atom (C2) also becomes a chiral center. Due to the inherent chirality of GSH and NAC, reaction of the cyclic chalcone analogs gives four isomeric adducts (Figure 2).

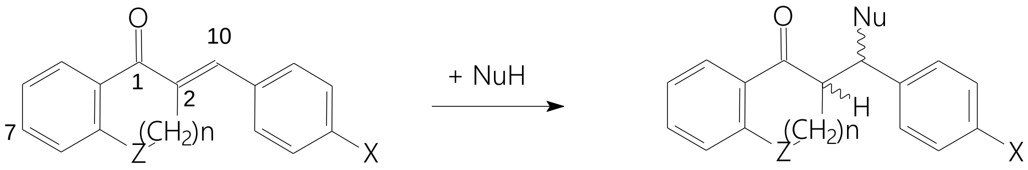

I n=0; Z=0: 2 stereoisomers; **II** n=1; Z= CH_2: 4 stereoisomers
III n=1; Z = O: 4 stereoisomers **IV** n=1; Z = $(CH_2)_2$: 4 stereoisomers
X = H (**a**), CH_3 (**b**), OCH_3 (**c**)

Figure 2. A simplified reaction scheme of addition of GSH and NAC onto chalcones (**I**) and cyclic chalcone analogs (**II-IV).** (Numbering refers to the carbocyclic derivatives.).

The reactions were conducted under three different pH conditions (pH 8,0, 6.3, and 3.2) to investigate how the ratio of the protonated to unprotonated forms of the thiol function affects the reactivity of the chalcones and the stereochemical outcome of the reactions. To quantitatively characterize the progress of the reactions and formation of the thiol-adducts, composition of the chalcone-thiol incubation mixtures was analyzed at the 15, 45, 75, 105, 135, 165, 195, 225, 255, 285, and 315-minute timepoints by HPLC-UV. For a better understanding of the kinetic features of the reactions, molecular modeling calculations were performed. These analyses used methanethiol (**CH_3SH**) and its deprotonated form (**CH_3S^-**) as model thiols.

Preprints.org (www.preprints.org) | NOT PEER-REVIEWED | Posted: 17 July 2024 doi:10.20944/preprints202407.1444.v1

2. Results

2.1. Reactions under Slightly Basic (pH 8.0) Conditions

Initially, the reactions of the three chromanones (**IIIa-c**) were investigated under basic (pH 8.0) conditions. Considering the p*K*a values of GSH (pK_a 8.83) and NAC (pK_a 9.52) [21], 12.8% of the GSH and 2.9% of the NAC molecules are in thiolate form under these conditions. These conditions were selected to mimic the GST-catalyzed reaction, in which ionization of the GSH-thiol function increases due to the interaction of the tripeptide with the G-site of the enzyme [22]. Under such conditions, GSH (Figure 3) and NAC (Figure 4) showed very high intrinsic reactivity with the investigated cyclic chalcone analogs (Tables 1 and 2).

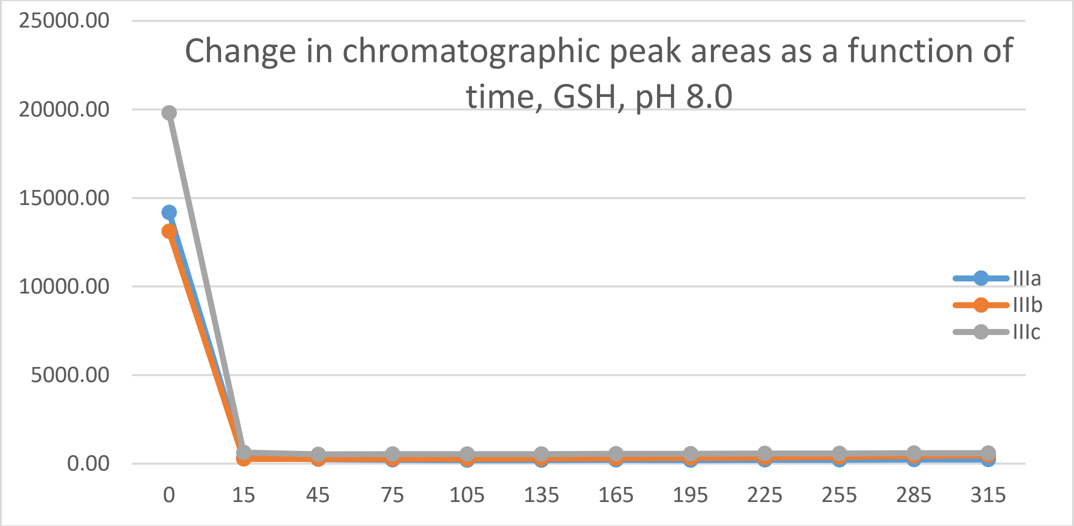

Figure 3. Change in the chromatographic peak area of chalcones **IIIa-c** as a function of time (min) in the chalcone/GSH incubations at pH 8.0.

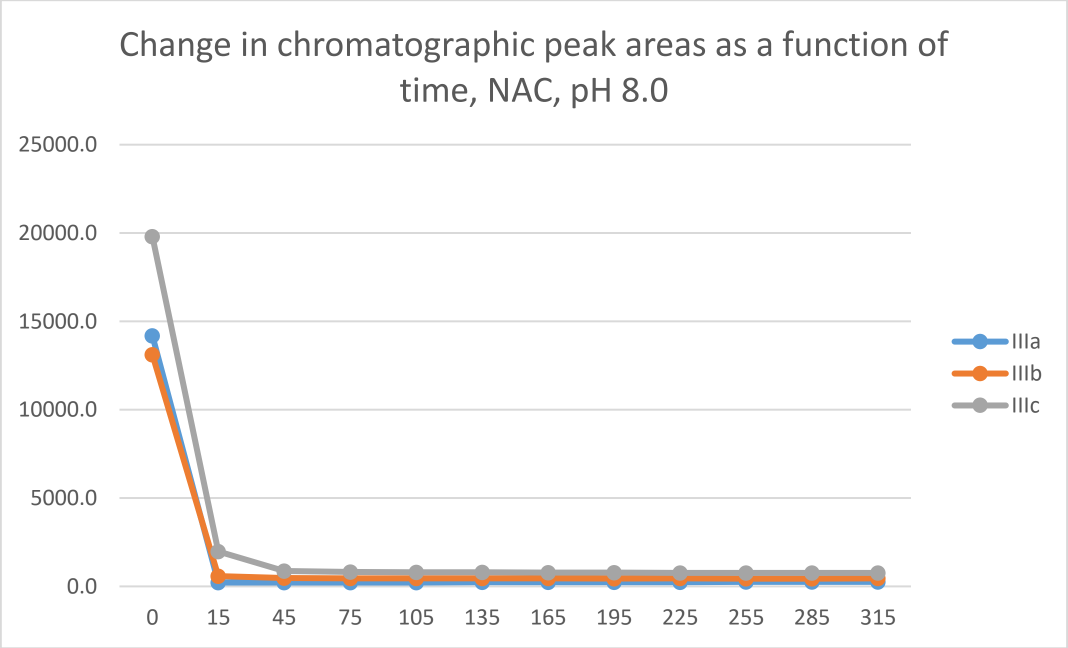

Figure 4. Change in the chromatographic peak area of chalcones **IIIa, IIIb,** and **IIIc** as a function of time (min) in the chalcone/NAC incubations at pH 8.0.

In all incubations, the peak area of the starting chalcones (**IIIa-c**) almost completely disappeared at the 45-minute timepoint. A comparison of the 15-minute and 45-minute peak areas of the NAC-incubates showed that **IIIc** was somewhat less reactive than **IIIa** and **IIIb**.

Table 1. Retention times (t_R)[1] and integrated peak areas (A) of the investigated cyclic chalcone analogs (**IIIa, IIIb,** and **IIIc**) and their GSH adducts[2].

pH[3]	Compound	t_R (*E*)-isomer	Area Ratio[4] A_{315}/A_0	t_R (*Z*)-isomer	t_R[2] GSH-1	Area GSH-1	t_R[2] GSH-2	Area GSH-2
3.2	**IIIa**	16.6	0.36	N.D.[5]	12.9	5346	13.2	4021
3.2	**IIIb**	17.1	0.42	N.D.[5]	14.6	3748	14.8	3472
3.2	**IIIc**	16.6	0.44	N.D.[5]	12.9	2136	13.4	1712
6.3	**IIIa**	16.6	0.02	N.D.[5]	12.3	12073	12.7	12421
6.3	**IIIb**	17.1	0.03	N.D.[5]	14.5	8028	14.7	10248
6.3	**IIIc**	16.6	0.03	N.D.[5]	13.0	9064	13.5	9315
8.0	**IIIa**	16.6	0.02	N.D.[5]	12.3	10330	12.7	12509
8.0	**IIIb**	17.0	0.03	N.D.[5]	14.4	5820	14.5	11685
8.0	**IIIc**	16.6	0.03	N.D.[5]	13.2	7615	13.6	10692

[1]Retention times in minutes; [2]Data refers to the average of two independent measurements at the 315 min time point; [3]pH value of the aqueous thiol solution; [4]Ratios of peak areas measured at 0 and 315 min; [5]Not detectable.

Earlier, formation of (Z)-isomers of chalcones **II** and **IV** was observed as a result of retro-Michael rection of the formed thiol-conjugates [1]. To investigate such a possibility in the present reactions, light-initiated (*E*)/(*Z*) isomerization of **IIIa-c** were performed [23]. The structure of the initial (*E*)- and the formed (*Z*)-isomers were identified by HPLC-MS (Figures S1-S9). HPLC-MS investigations indicated no sign of formation of (Z)-isomers in any of the studied incubations. (The isomers did not separate under the HPLC-UV conditions.)

Table 2. Retention times (t_R)[1] and integrated peak areas (A) of the investigated cyclic chalcone analogs (**IIIa, IIIb,** and **IIIc**) and their NAC adducts[2].

pH[3]	Compound	t_R (*E*)-isomer	Area Ratio[4] A_{315}/A_0	t_R[2] (*Z*)-isomer	t_R NAC-1	Area[2] NAC-1	t_R NAC-2	Area[2] NAC-2
3.2	**IIIa**	16.7	0.262	N.D.[5]	15.1	9483	N.D.	N.D.
3.2	**IIIb**	17.2	0.267	N.D.[5]	15.9	6333	N.D.	N.D.
3.2	**IIIc**	16.7	0.315	N.D.[5]	15.2	8088	N.D.	N.D.
6.3	**IIIa**	16.6	0.025	N.D.[5]	15.1	10347	N.D.	N.D.
6.3	**IIIb**	17.1	0.044	N.D.[5]	15.9	18353	N.D.	N.D.
6.3	**IIIc**	16.6	0.054	N.D.[5]	15.0	3987	15.2	11003
8.0	**IIIa**	16.6	0.017	N.D.[5]	15.0	20271	N.D.	N.D.
8.0	**IIIb**	17.1	0.035	N.D.[5]	15.9	19590	N.D.	N.D.
8.0	**IIIc**	16.7	0.038	N.D.[5]	15.1	8099	15.2	10006

[1]Retention times in minutes; [2]Data refers to the average of two independent measurements at the 315 min time point; [3]pH value of the aqueous thiol solution; [4]Ratios of peak areas measured at 0 and 315 min; [5]Not detectable.

As a result of the reactions, two new chiral centers are formed in the products. Under our chromatographic conditions, however, appearance of four peaks could not be observed. In the case of the GSH-incubations, two chromatographic peaks with similar retention times were detected (Table 1). The structure of the adducts was supported by HPLC-MS (Figures S11-S27). The 315-minute ratio of GSH-1/GSH-2 peak areas of **IIIa**, **IIIb,** and **IIIc** is 0.83, 0.50 and 0.71, respectively. The ratio of the two peaks did not change as a function of time (Figures 5 and 6).

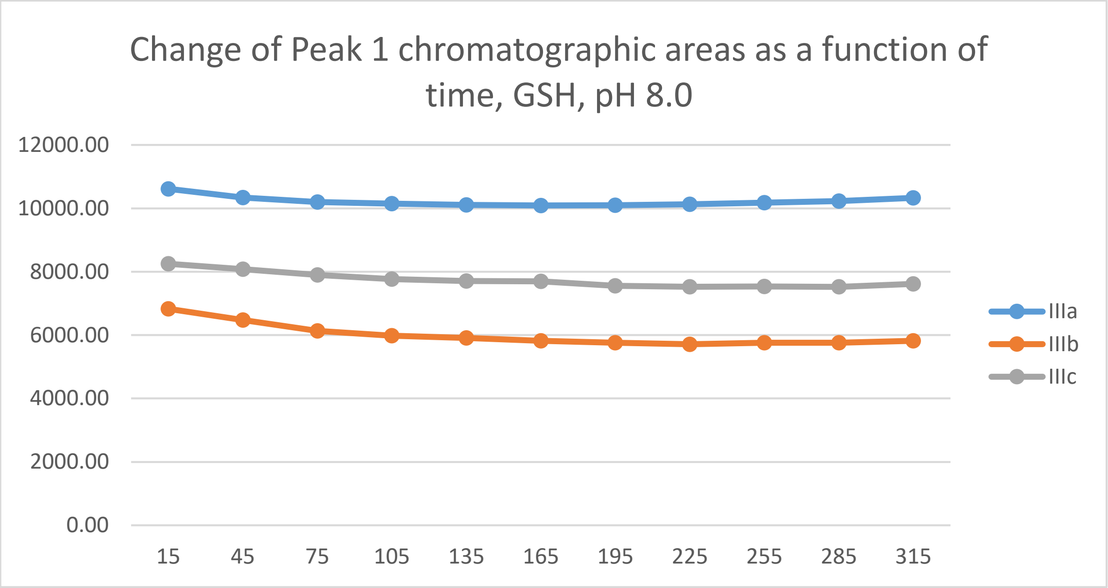

Figure 5. Change in the chromatographic peak area of adduct-1 of **IIIa, IIIb**, and **IIIc** as a function of time (min) in the chalcone/GSH incubations at pH 8.0.

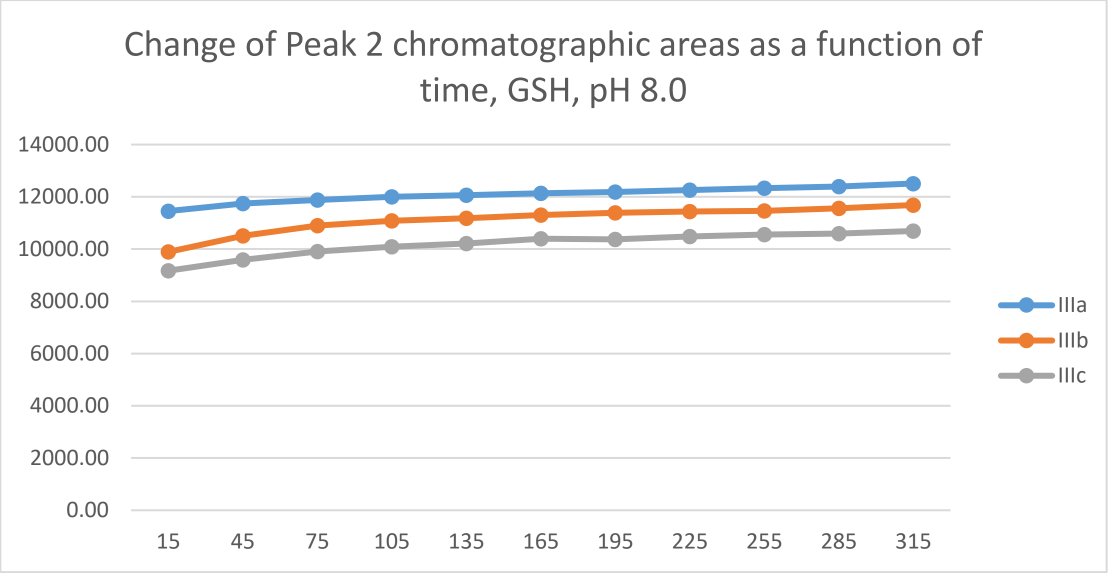

Figure 6. Change in the chromatographic peak area of adduct-2 of **IIIa, IIIb,** and **IIIc** as a function of time (min) in the chalcone/GSH incubations at pH 8.0.

Analysis of the NAC-incubations showed only one chromatographic peak in the **IIIa**- and **IIIb** incubates. Two chromatographic peaks could only be observed for the **IIIc** incubate (Figures 7 and 8). The structure of the formed chalcone-NAC adducts was supported by HPLC-MS (Figures S28-36). The 315-minute ratio of the **IIIc** NAC-1/NAC-2 (0.81) peaks is similar to that of the GSH-1/GSH-2 (0.71) (Tables 1 and 2).

doi:10.20944/preprints202407.1444.v1

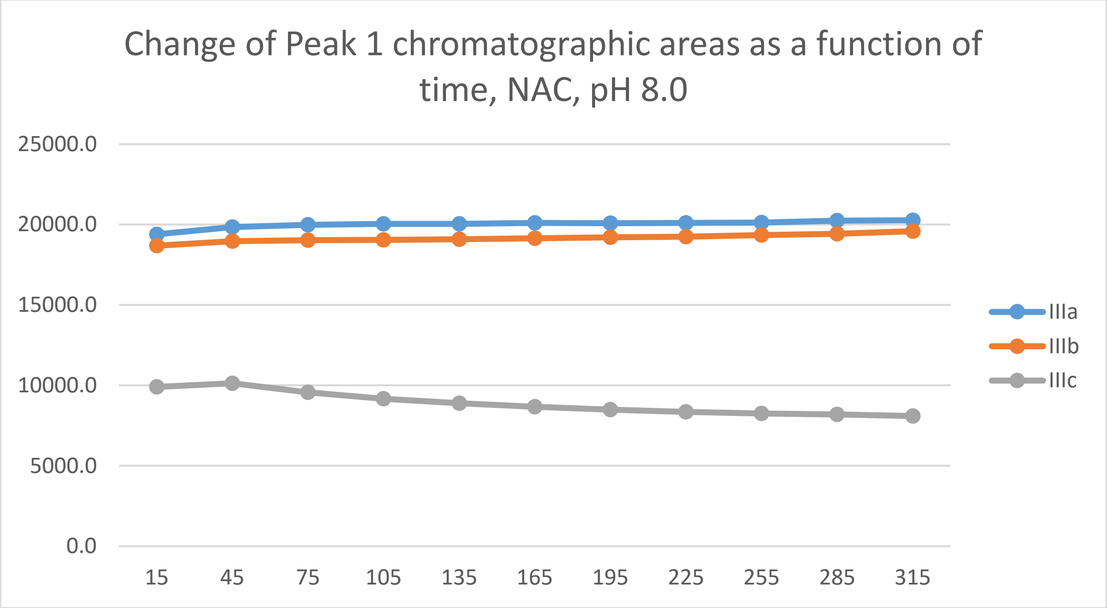

Figure 7. Change in the chromatographic peak area of adduct-1 of **IIIa, IIIb,** and **IIIc** as a function of time (min) in the chalcone/NAC incubations at pH 8.0.

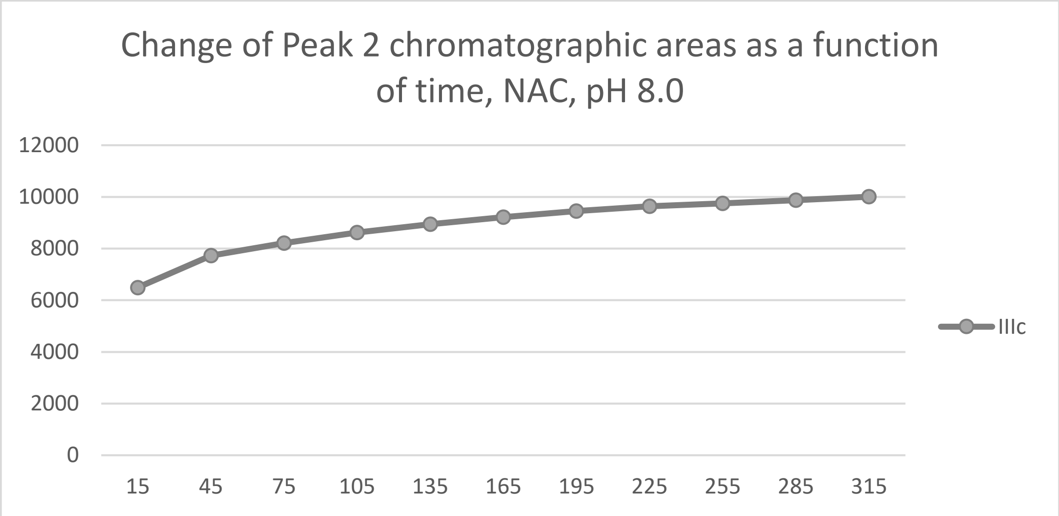

Figure 8. Change in the chromatographic peak area of adduct-2 of **IIIc** as a function of time (min) in the chalcone/NAC incubations at pH 8.0.

2.2. Reactions under Slightly Acidic (pH 6.3) Conditions

Reactions under slightly acidic conditions mimic the cellular milieu of the cancer cells [24]. Under such conditions, about 0.3% of the GSH molecules and 0.06% of the NAC molecules exist in the more reactive thiolate form. According to the expectations, the progress of the reactions under such conditions is slower than that observed at pH 8.0.

In the GSH incubations, the reaction of compounds **IIIa** and **IIIb** at the 105-minute and **IIIc** at the 255-minute timepont reached the equilibrium state. Reactivity of the methoxy-substituted derivative (**IIIc**) was slower than that of **IIIa** and **IIIb** (Figure 9). Difference in reactivity of **IIIa-c** became more pronounced in the NAC-incubates. Reactivity of the substituted derivatives (**IIIb** and **IIIc**) was lower than the unsubstituted **IIIa** (Figure 10).

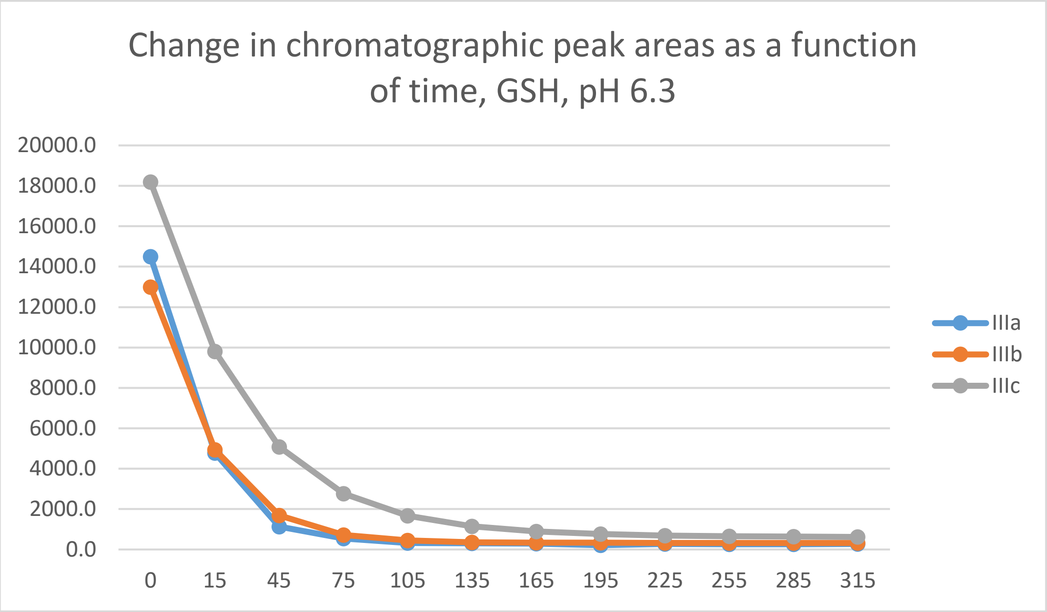

Figure 9. Change in the chromatographic peak area of chalcones **IIIa-c** as a function of time (min) in the chalcone/GSH incubations at pH 6.3.

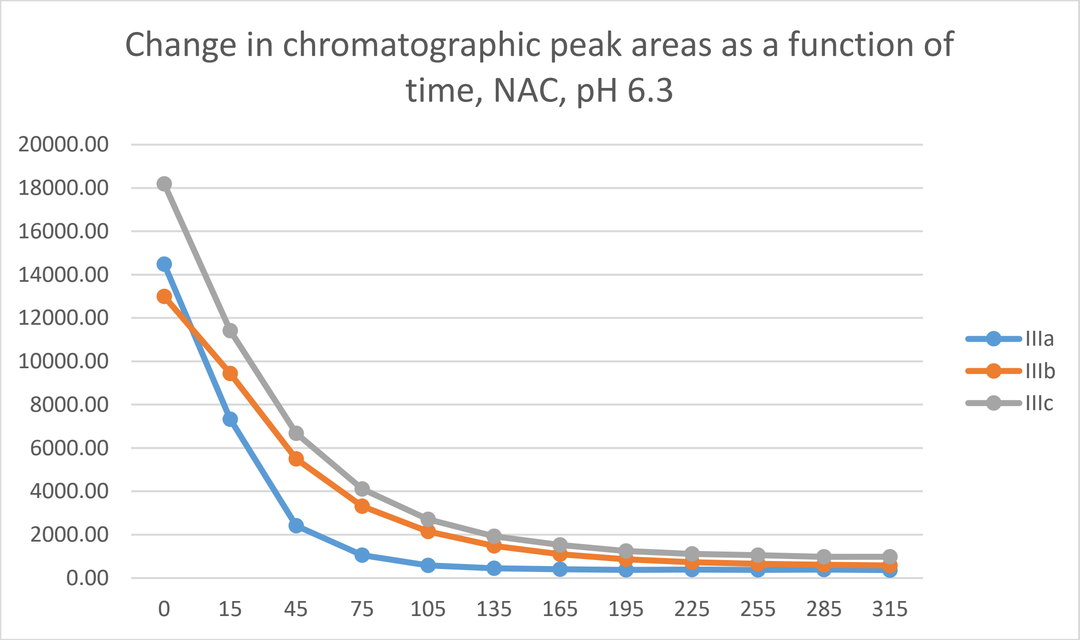

Figure 10. Change in the chromatographic peak area of chalcones **IIIa-c** as a function of time (min) in the chalcone/NAC incubations at pH 6.3.

The HPLC chromatographic profile of the formed GSH- and NAC-conjugates (Figures 11-14) is similar to that of the pH 8.0 ones (Figures 5-8). The 315-minute ratio of GSH-1/GSH-2 peak areas of **IIIa**, **IIIb,** and **IIIc** is 0.97, 0.78, and 0.97, respectively (Table 2). The 315-minute ratio of the **IIIc** NAC-1/NAC-2 peaks (0.36), however, is very different from that of the GSH-1/GSH-2 peaks (0.97) (Tables 1 and 2).

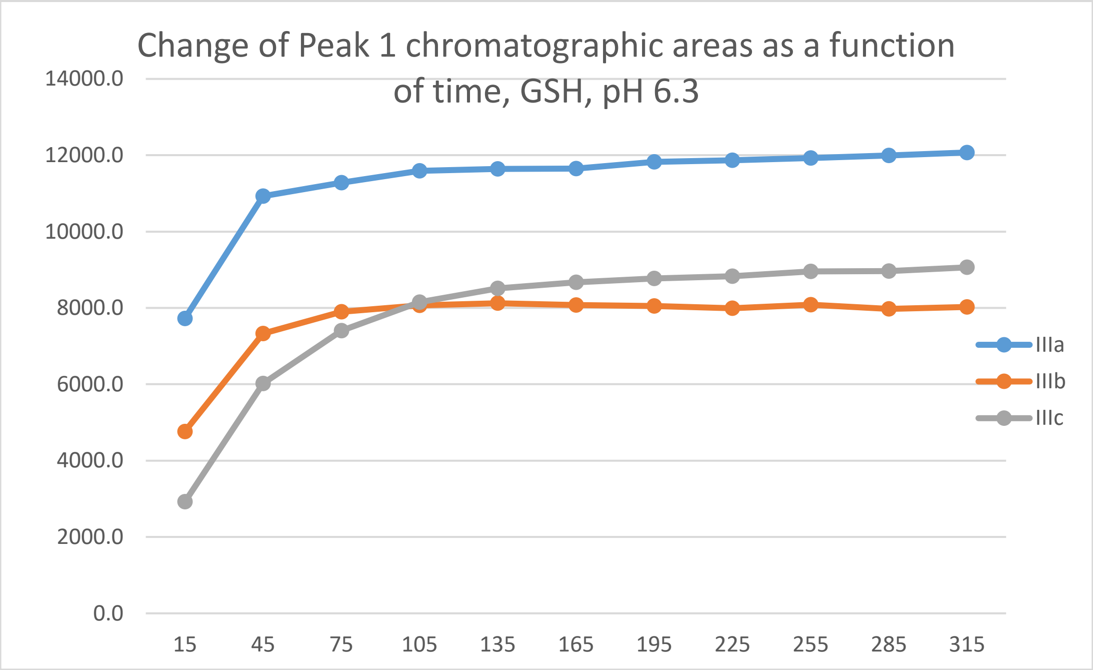

Figure 11. Change in the chromatographic peak area of adduct-1 of **IIIa, IIIb,** and **IIIc** as a function of time (min) in the chalcone/GSH incubations at pH 6.3.

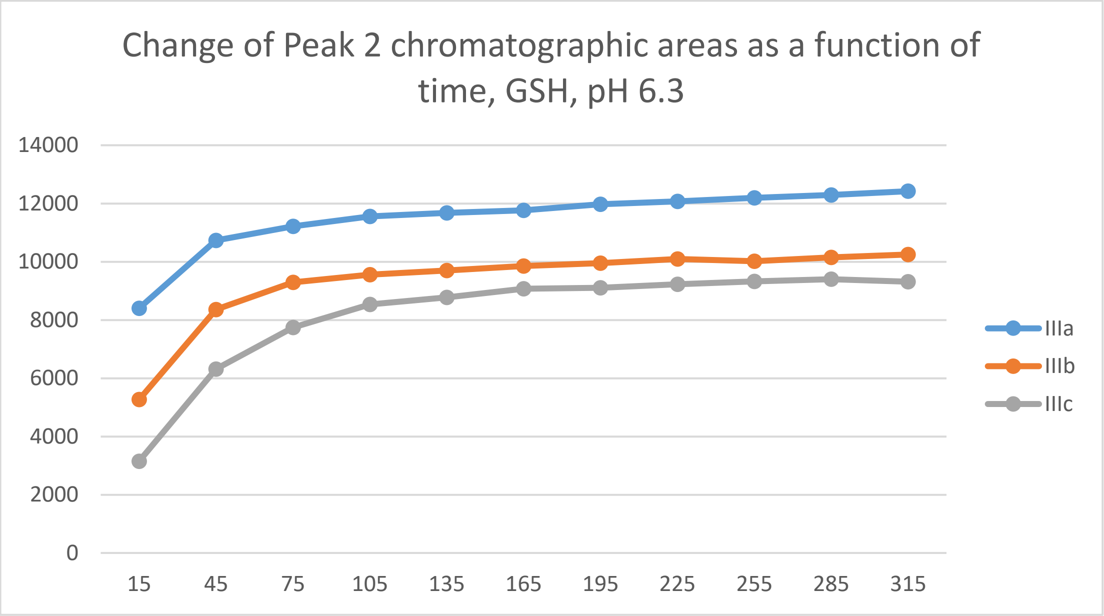

Figure 12. Change in the chromatographic peak area of adduct-2 of **IIIa, IIIb,** and **IIIc** as a function of time (min) in the chalcone/GSH incubations at pH 6.3.

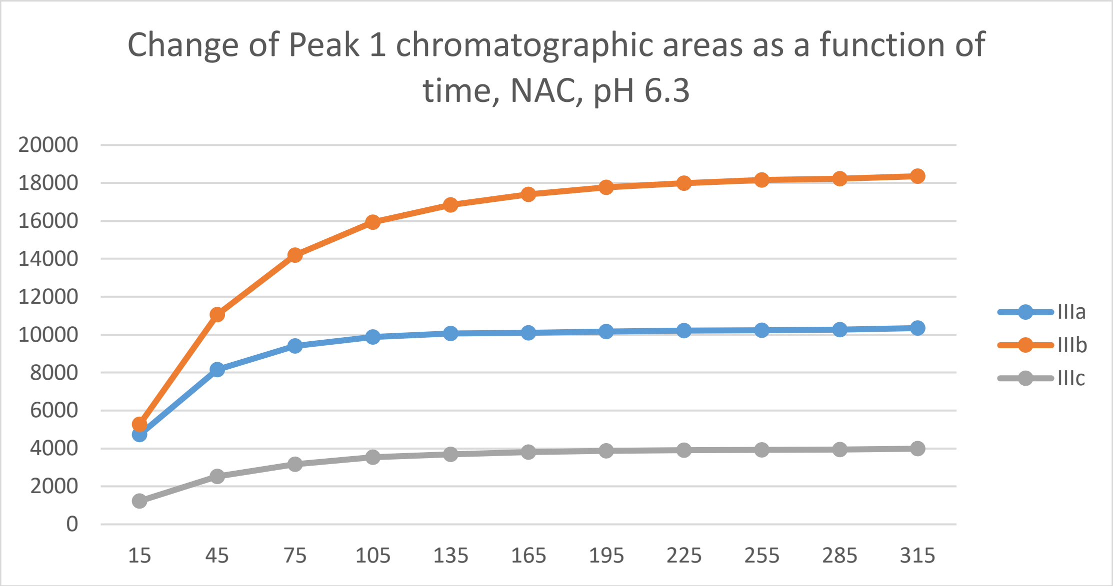

Figure 13. Change in the chromatographic peak area of adduct-1 of **IIIa, IIIb,** and **IIIc** as a function of time (min) in the chalcone/NAC incubations at pH 6.3.

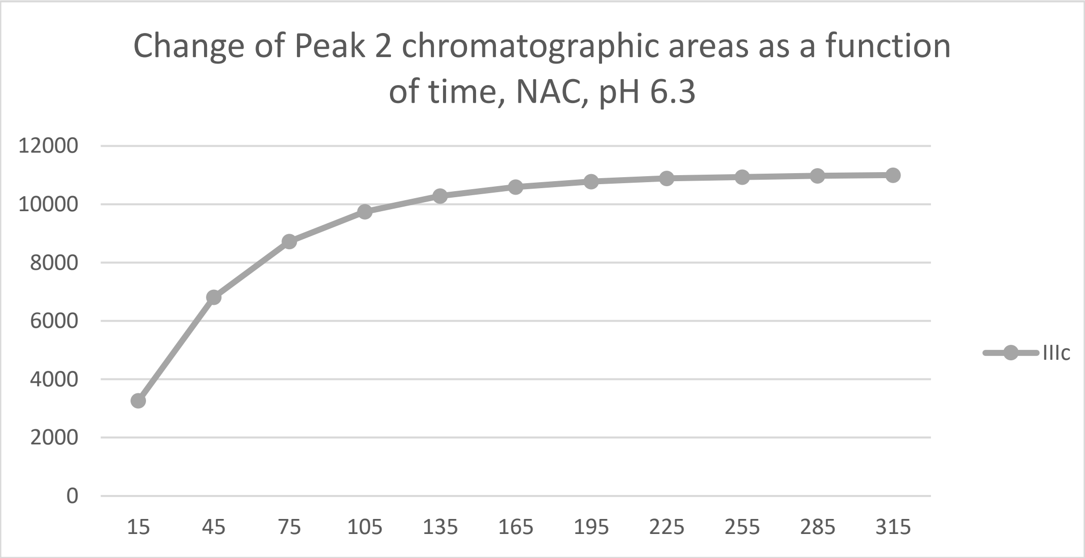

Figure 14. Change in the chromatographic peak area of adduct 1 of **IIIa, IIIb,** and **IIIc** as a function of time (min) in the chalcone/NAC incubations at pH 6.3.

2.3. Reactions under Acidic (pH 3.2) Conditions

Under strongly acidic conditions, the thiol function of GSH and NAC is fully protonated. According to the reduced reactivity of the protonated thiol nucleophiles, the initial area of the HPLC peak of **IIIa**-**c** was decreased by much smaller extents (Tables 1 and 2). The progression curves of the three derivatives run parallel in both thiol incubations. Similar to the previous results, the methoxy derivative (**IIIc**) also showed the lowest reactivity under such conditions (Figures 15 and 16).

Preprints.org (www.preprints.org) | NOT PEER-REVIEWED | Posted: 17 July 2024 doi:10.20944/preprints202407.1444.v1

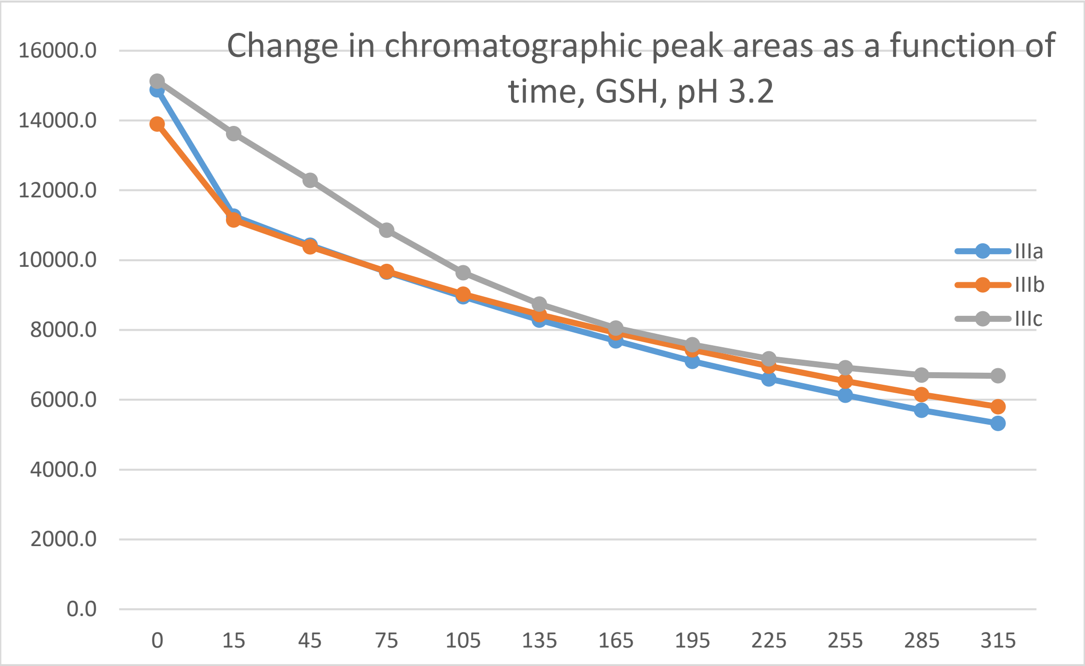

Figure 15. Change in the chromatographic peak area of chalcones **IIIa-c** as a function of time (min) in the chalcone/GSH incubations at pH 3.2.

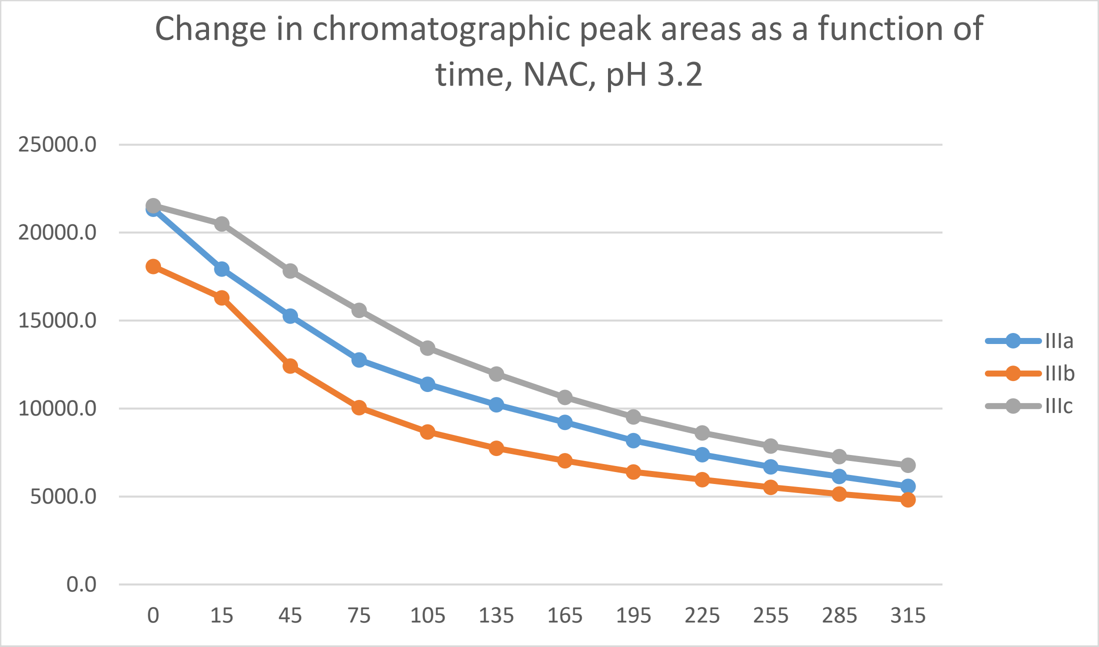

Figure 16. Change in the chromatographic peak area of chalcones **IIIa-c** as a function of time (min) in the chalcone/NAC incubations at pH 3.2.

Similar to the previous results, two chalcone-GSH and one chalcone-NAC peak could be detected in the incubates. The peak areas of the GSH-1 and GSH-2 conjugates showed a linear increase with different slopes for the three derivatives (Figures 17 and 18). The 315-minute ratio of GSH-1/GSH-2 peak areas of **IIIa**, **IIIb,** and **IIIc** is 1.3, 1.1 and 1.2, respectively (Table 2). HPLC analysis of the NAC incubates showed only one adduct peak in the case of each compound (Figure 19).

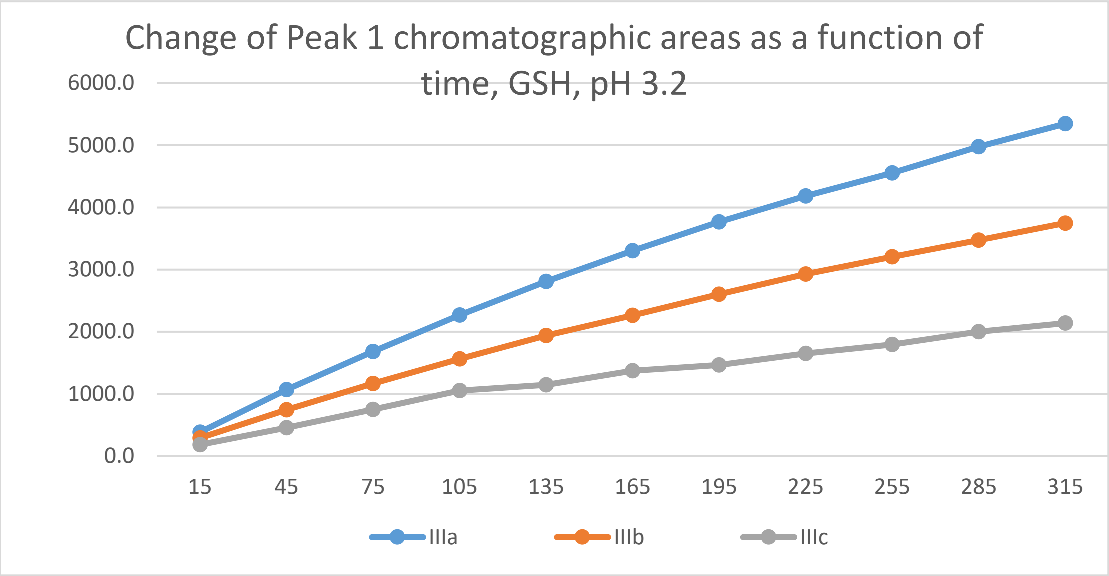

Figure 17. Change in the chromatographic peak area of adduct-1 of **IIIa, IIIb,** and **IIIc** as a function of time (min) in the chalcone/GSH incubations at pH 3.2.

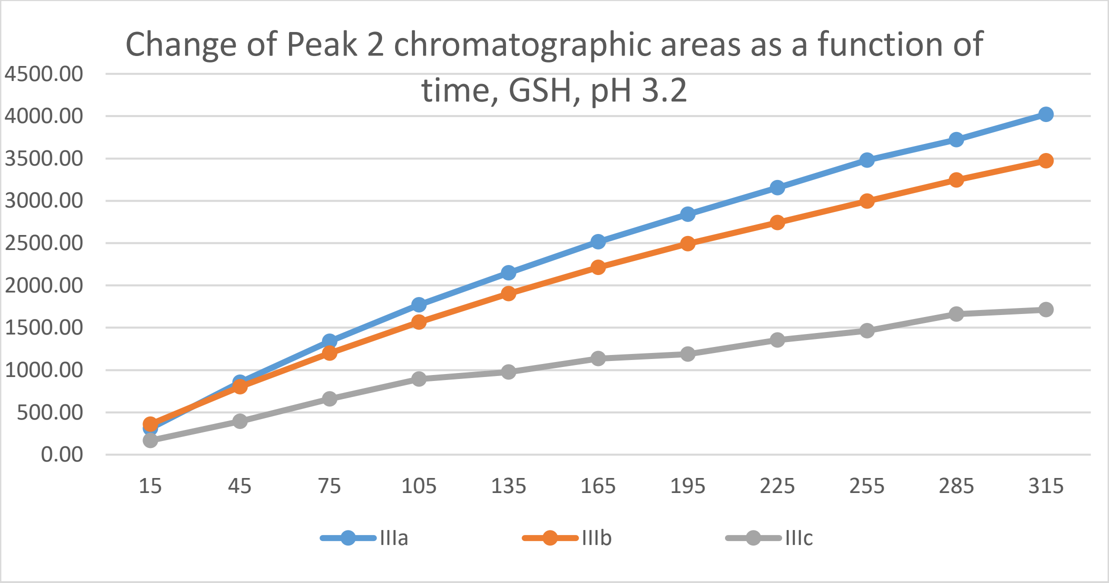

Figure 18. Change in the chromatographic peak area of adduct-2 of **IIIa, IIIb,** and **IIIc** as a function of time (min) in the chalcone/GSH incubations at pH 3.2.

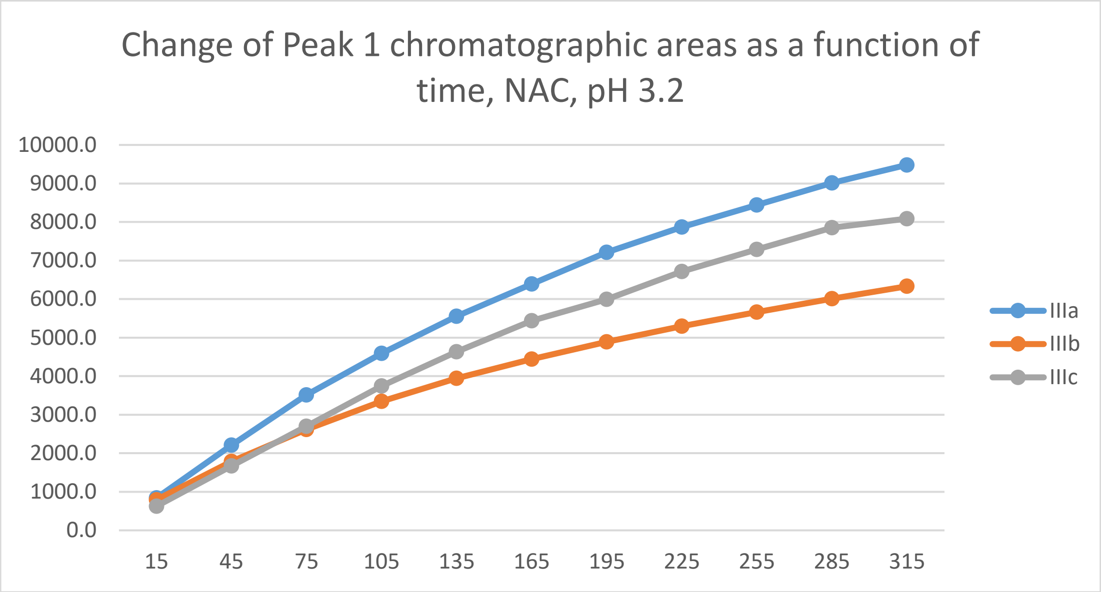

Figure 19. Change in the chromatographic peak area of adduct-1 of **IIIa, IIIb,** and **IIIc** as a function of time (min) in the chalcone/NAC incubations at pH 3.2.

2.4. Molecular Modeling Analysis

Table 3 shows the calculated values for molecular properties of **Ia**, **IIa**, **IIIa, IVa,** methanethiol (**CH_3SH**), and deprotonated methanethiol (**CH_3S^-**). The difference between the HOMO energy of **CH_3SH** and **CH_3S^-** is spectacular, indicating the much higher nucleophilicity of the deprotonated thiol. The LUMO energy of the analogous carbocyclic chalcones (**Ia**, **IIa**, and **IVa**) increases parallel with the ring size (Table 3). The HOMO and LUMO plots of compounds **IIa** and **IIIa** are shown in Figure 20. The values and coefficients of the LUMO orbital are similar in the two compounds.

Table 3. Reactivity indices were obtained for **2a**, **3a, CH_3SH,** and **CH_3S^-** at the M06-2X/6-311++G(d,p) level of theory.

Descriptor	**Ia kcal.mol^{-1}**	**IIa kcal.mol^{-1}**	**IIIa kcal.mol^{-1}**	**IVa kcal.mol^{-1}**	**CH_3SH kcal.mol^{-1}**	**CH_3S^- kcal.mol^{-1}**
E_{HOMO}	-183.24	-181.22	-182.43	-180.38	-183.24	-173.45
E_{LUMO}	-35.98	-31.57	-28.44	-28.44	-2.98	77.80
$\Delta E_{HOMO-LUMO}$	147.26	149.65	153.99	151.94	180.26	251.27
Chemical Potential (μ)	-109.61	-104.83	-105.44	-104.405	-93.11	47.73
Chemical Hardness (η)	147.26	149.65	153.99	151.94	-180.26	-251.27
Electrophilicity Index (ω)	40.79	35.96	36.10	35.87	-24.05	4.53

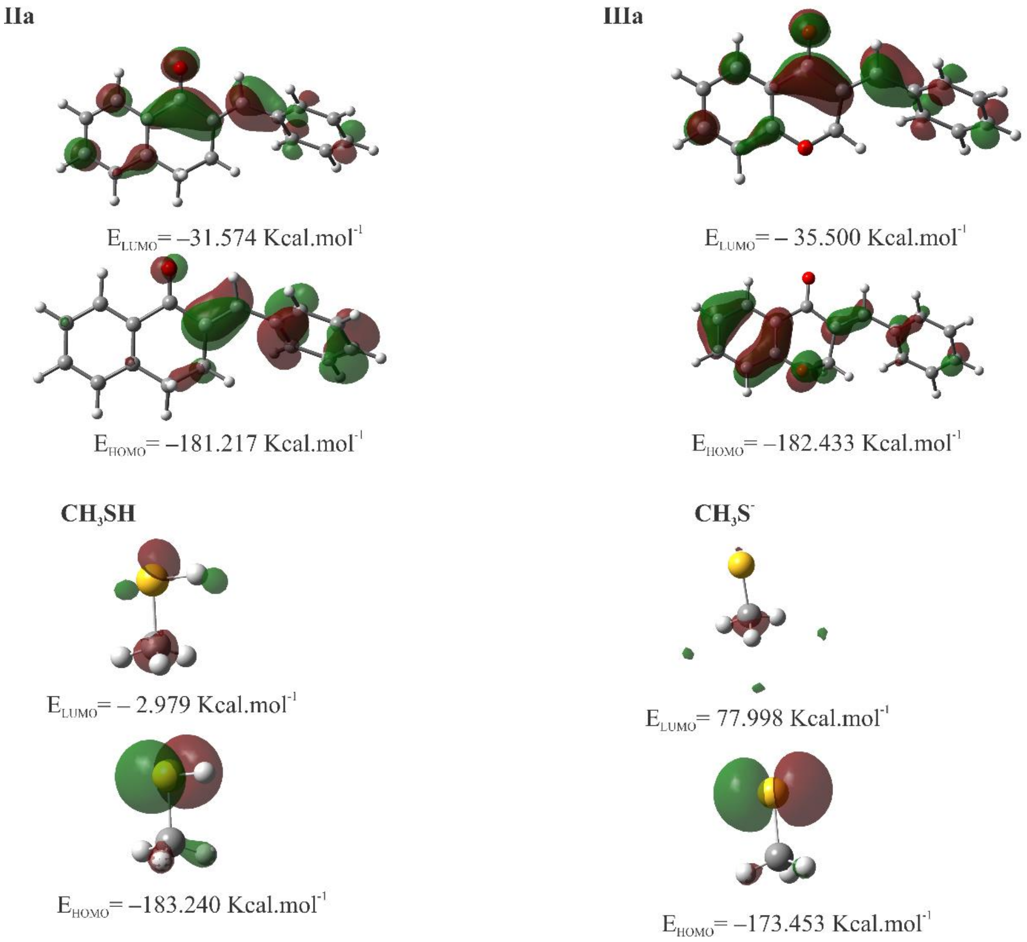

Figure 20. HOMO and LUMO plots of **IIa**, **IIIa**, **CH$_3$SH**, and **CH$_3$S$^-$** calculated at the M06-2X/6-311++G(d,p) level of theory.

According to the analysis of the condensed Fukui functions, the orientation of the nucleophilic attack varies in response to different values of $\Delta f(r)$. Specifically, if $\Delta f(r) > 0$, the site will likely undergo a nucleophilic attack. Conversely, if $\Delta f(r) < 0$, the site is favored for an electrophilic attack.

To visualize the relative charge distribution on the molecular surface, molecular electrostatic potential (MEP) mapping was carried out (Figure 21). The red spots on the MEP surface represent the electron-rich sites on the surface of the molecules and are susceptible to electrophilic attack. In contrast, the blue spots represent the electron-depleted regions and are sites susceptible to nucleophilic attack. For **CH$_3$S$^-$**, the MEP is reddish due to the unit negative charge resulting from deprotonation.

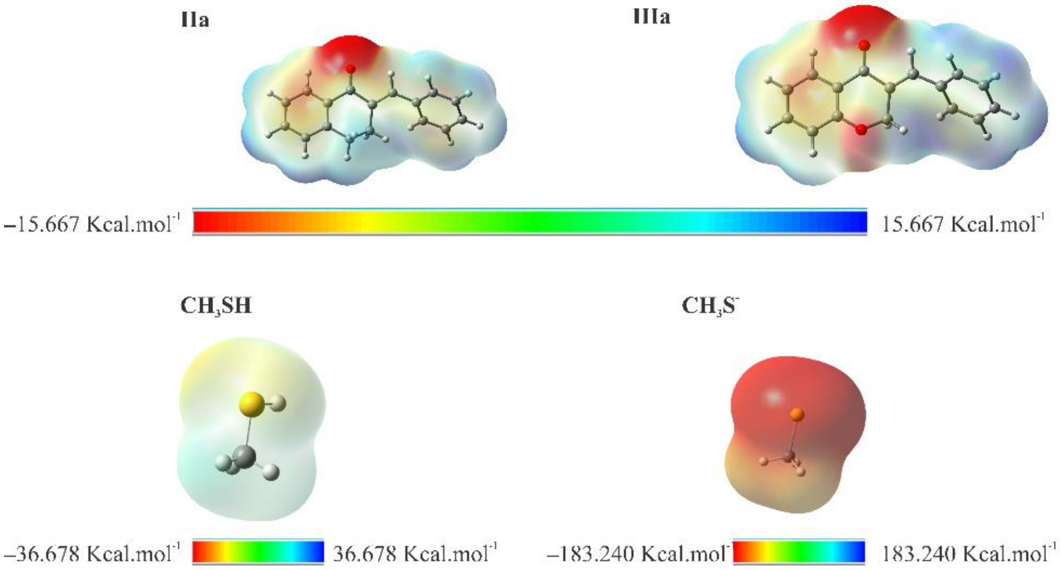

Figure 21. MEP surface at $\varrho(r) = 4.0 \times 10^{-4}$ electrons/Bohr3 contour of the total SCF electronic density for molecules **IIa**, **IIIa**, **CH_3SH**, and **CH_3S^-** at the M06-2X/6-311++G(d,p) level of theory.

Furthermore, a series of electronic structure calculations using the Density Functional Theory (DFT) method was performed to obtain the transition states (TS) for the reaction of methanethiolate (**CH_3S^-**) with the two chalcones analogs, **IIa** and **IIIa**. For the transition state involving **IIIa**, formation of three hydrogen bonds is observed, as identified by the critical points obtained through the Quantum Theory of Atoms in Molecules (QTAIM) methodology. The C-S bond formed in the transition state of **IIIa** exhibits a strong character; in contrast, **IIa** has a moderate one. This difference suggests greater stability for the transition state of **IIIa**. Analyzing the distortion of the six-membered rings, it was found that in **IIIa**, the oxygen atom shifts to an envelope, while in **IIa, it** has a skew boat conformation (Figure 22, panel a).

Evaluating the frontier orbitals (HOMO and LUMO) of the transition states, it is found that the energy gap is approximately equal for both compounds (Figure 20, panel b), indicating that energetics is not a predominant factor in differentiating the reactivity between the compounds. On the contrary, the Gibbs free energy profile showed characteristic differences. For **IIIa**, the energy barrier is 10.5 kcal.mol^{-1}, while for **IIa**, it is 17.1 kcal.mol^{-1}. Thermodynamically, the product formed from **IIIa** is more stable than that formed from **IIa** with a Gibbs free energy of -10.4 kcal.mol^{-1} and 5.7 kcal.mol^{-1}, respectively (Figure 22, panel c).

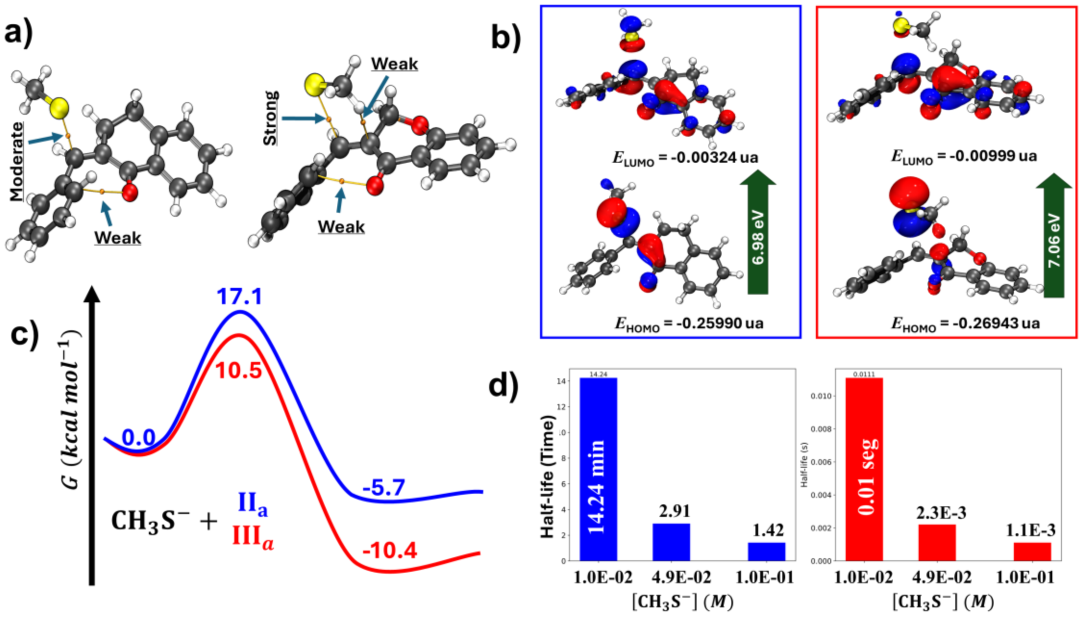

Figure 22. Results on the methanethiolate (**CH_3S^-**) addition to **IIa** and **IIIa** showing structural, energetic, and kinetic analysis of the transition states (TS). (a) TS for the reaction of **CH_3S^-** with **IIa** and **IIIa**. Arrows indicate the strength of interactions. (b) Frontier orbitals (HOMO and LUMO) of TSs of **IIa** and **IIIa**. (c) Gibbs free energy profile for the reactions of **IIa** and **IIIa**. (d) Kinetic analysis showing the half-life of the reactions of **IIa** (blue bars) and **IIIa** (red bars) with different methanethiolate concentrations.

Using a pseudo-first-order approximation, the half-lives of the two reactions were calculated. For an excess concentration of 4.9 x 10^{-2} M of methanethiolate, the estimated half-life for the reaction for **IIa** is approximately 2.91 minutes, while for **IIIa**, it is 2.3 x 10^{-3} seconds (Figure 22, panel d).

3. Discussion

In our earlier studies, the thiol reactivity of some chalcones (**I**) [20] and the carbocyclic chalcone analogs **II** [1] and **IV** [25] were investigated. It was found that the carbocyclic chalcone analogs (**II** and **IV**) had lower thiol-reactivity than the respective open-chain (**I**) ones. Figure 23 shows the progression curves of the reactions of the investigated methyl(**b**)- and methoxy(**c**)-substituted chalcones/cyclic chalcone analogs (**I-IV**) with GSH under basic (pH 8.0) conditions. Such a comparison shows that the seven-membered analogs (**IV c** and **IV b**) have much lower thiol-reactivity than the respective open-chain (**I**) and chromanone (**III**) derivatives. Furthermore, comparing the GSH-reactivity of **IIb,c** with **IIIb,c** showed the chromanone analogs (**III**) to have much higher reactivity than the respective carbocyclic tetralones (**II**).

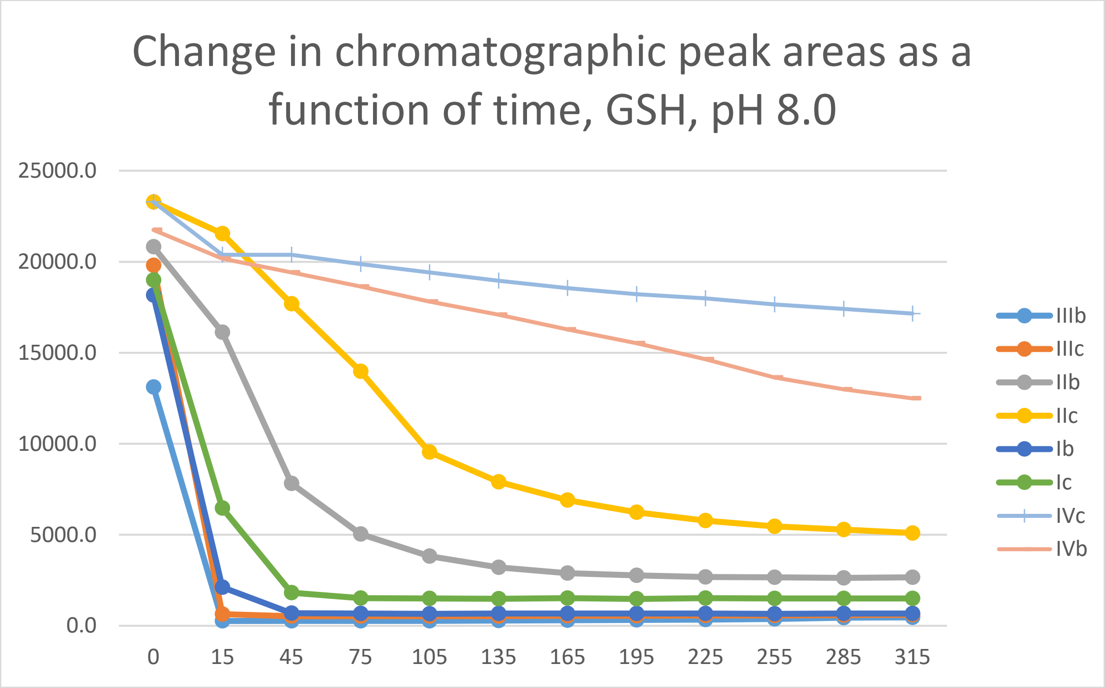

Figure 23. Comparison of change of chromatographic peak areas of selected chalcones (**Ib**, **Ic**) and cyclic chalcone analogs (**IIb**, **IIc**; **IIb**, **IIc**; and **IVb**, **IVc**) as a function of time (min) in the chalcone/GSH incubations, pH 8.0.

Similar observation could be made by comparison of the respective progression curves of the reactions between the above chalcones and NAC under pH 8.0 conditions. Like in the case of GSH, the seven-membered cyclic analogs (**IVb** and **IVc**) showed the lowest reactivity. Reactivity of the open-chain chalcones (**Ib** and **Ic**) was comparable with that of the chromanone analogs **IIIb** and **IIIc** (Figure 24). The higher thiol p*K*a value of NAC is reflected by the lower reaction and conversion rate of the two carbocyclic analogs **IIb,c** and **IVb,c** compared to those with GSH (Figures 23 and 24).

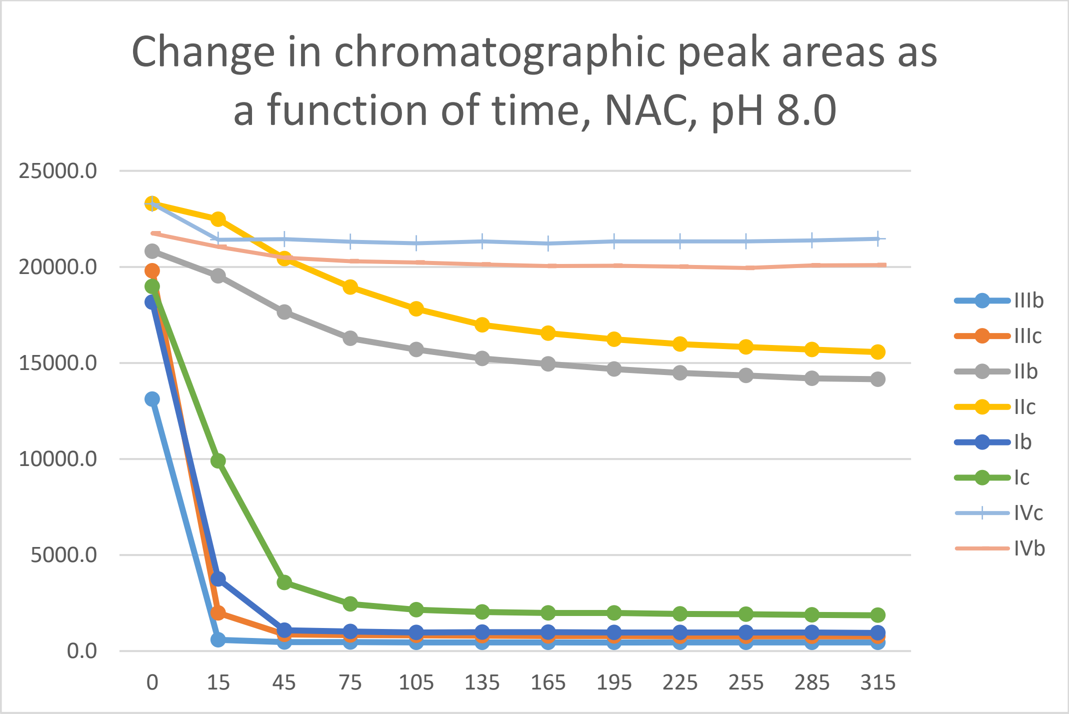

Figure 24. Comparison of change of chromatographic peak areas of selected chalcones (**Ib**, **Ic**) and cyclic chalcone analogs (**IIb**, **IIc**; **IIb**, **IIc**; and **IVb**, **IVc**) as a function of time (min) in the chalcone/NAC incubations, pH 8.0.

The differences observed in the reactivity of compounds **II** and **III** are more distinct in the GSH- and NAC-incubations carried out under the slightly acidic conditions (pH 6.3). Under such conditions, the chromanone derivatives (**IIIb,c**) showed the highest reactivity, followed by somewhat lower one of the open-chain chalcones (**Ib,c**) (Figures 25 and 26). The methyl-substituted (**b**) derivatives showed higher reactivity than the methoxy-substituted (**c**) ones in each series. Under these slightly acidic conditions, reactivity of the two carbocyclic chalcone analogs (**II** and **IV**) was substantially reduced and displayed similar reactivity.

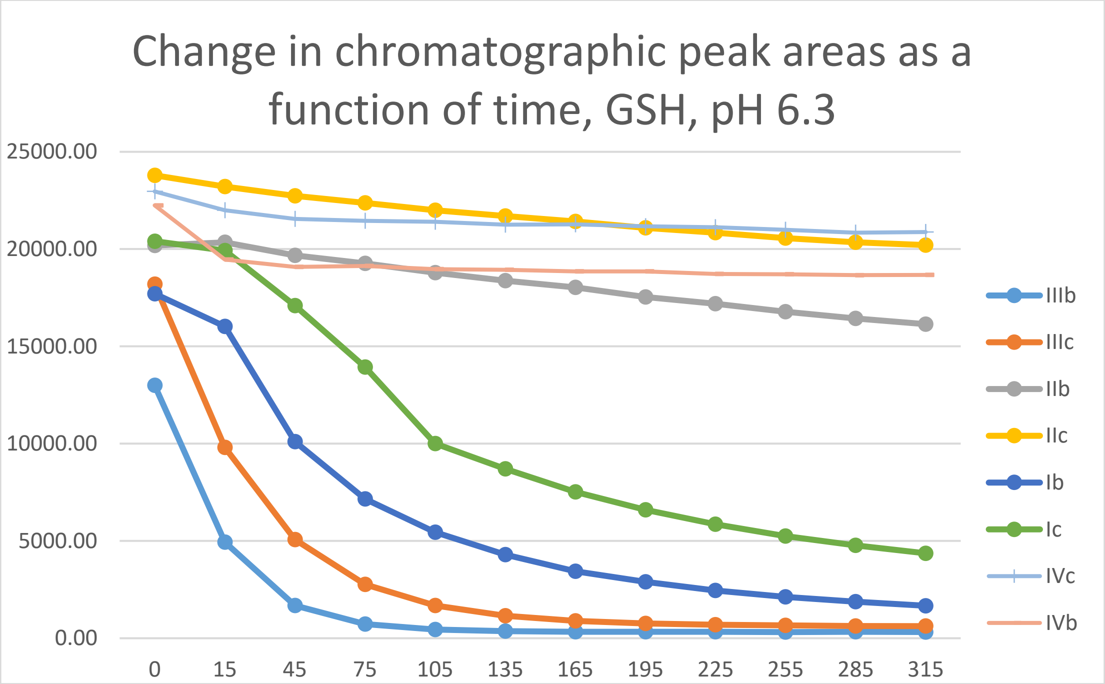

Figure 25. Comparison of change of chromatographic peak areas of selected chalcones (**Ib**, **Ic**) and cyclic chalcone analogs (**IIb**, **IIc**; **IIb**, **IIc**; and **IVb**, **IVc**) as a function of time (min) in the chalcone/GSH incubations, pH 6.3.

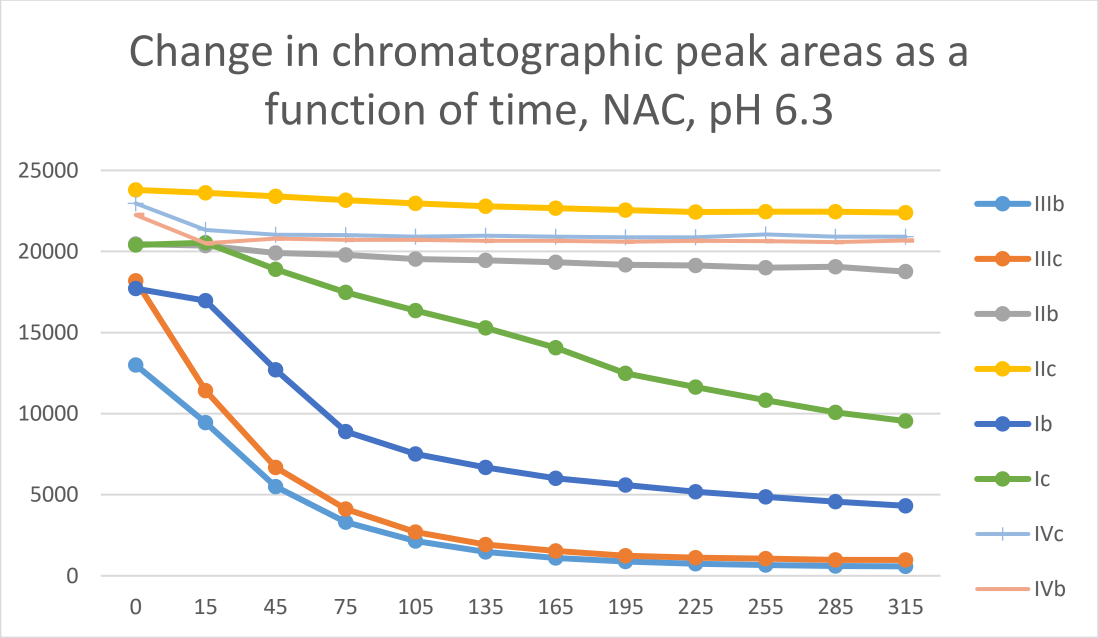

Figure 26. Comparison of change of chromatographic peak areas of selected chalcones (**Ib**, **Ic**) and cyclic chalcone analogs (**IIb**, **IIc**; **IIb**, **IIc**; and **IVb**, **IVc**) as a function of time (min) in the chalcone/NAC incubations, pH 6.3.

Similar observations were made while investigating the GSH-reactivity of the four series (**I**-**IV**) under pH 3.2 conditions. Under such acid conditions, the reactivity of the open-chain (**I**) and the carbocyclic (**II** and **IV**) analogs is much lower than those of the chromanones **IIIb** and **IIIc** (Figures S37 and S38).

In the thia-Michael reactions, the HOMO electron pairs of the nucleophile (**CH_3SH** or **CH_3S^-**) react with the empty LUMO of the electrophile. The closer in energy these two orbitals are located, the greater energy stabilization is obtained during the reactions [26]. In addition to the **IIa** and **IIIa**, the previously published molecular modeling parameters of the open-chain **Ia** and the seven-membered analog **IV**a have also been incorporated into Table 3. According to the calculated data, the observed thiol-reactivities of the open-chain **I** and the carbocyclic **II** and **IV** derivatives (Figures 23 and 24) showed good parallelism with increased LUMO energies of the three series. However, the LUMO energy of the least reactive **IV** and the most reactive **III** derivatives are the same (Table 3). Accordingly, the difference in the E_{LUMO} values of **IIa** and **IIIa** (-31.57 kcal/mol and -28.44 kcal/mol, respectively) does not justify the much higher reactivity of **IIIa**.

According to the experimental results and the condensed Fukui functions of **Ia** [20], **IVa** [25], **IIa,** and **IIIa** (Table 4), the preferred site of the nucleophilic attack is the beta (C10, and in **IIIa**-c compounds, C3a), carbon atom**.** The ground state relative electrophilicity of the beta-carbon atoms can be reflected by their ^{13}C NMR chemical shifts [27]. Table 5 summarizes the ^{13}C NMR chemical shifts of the carbon atoms of the enone moiety of **Ia**, **IIa-c**, **IIIa-c,** and **IVa**. As shown, the electron density (^{13}C NMR shifts) of the C10 atoms are relatively close to each other in all the cyclic chalcone analogs (**II**, **III,** and **IV**). The only exception is the open-chain **Ia**. The reduced electron density of the beta (C10) carbon atom, the high polarity of the C=C bond, and the conformational flexibility of the reaction intermediate can be considered to be the basis of the higher reactivity of compounds **I** than the C2-substituted, conformationally less flexible carbocyclic **II** and **IV**.

Table 4. Condensed Fukui function for **IIa** and **IIIa.** (For numbering, see Figure 1 and Table 5.).

		IIa				IIIa	
Atom	*f-*	*f+*	Δ*f*	**Atom**	*f-*	*f+*	Δ*f*
C1	0.011	0.098	0.087	**C4**	0.004	0.093	0.089
O(=C)	0.053	0.114	0.060	**O(=C)**	0.039	0.111	0.072
C7	0.029	0.060	0.032	**C3**	0.013	0.038	0.025
C10	0.062	0.082	0.020	**C3a**	0.043	0.086	0.043

Table 5. ^{13}C NMR chemical shifts (ppm; in $CDCl_3$) of the carbon atoms of the enone moiety of **Ia**, **IIa-c**, **IIIa-c,** and **IV**.

Compound$^{\text{Reference}}$	**δC1*(C4**)**	**δC2*(C3**)**	**δC10*(C3a**)**	**Δ(δ(C10/*C3a**)-δ(C2*/C3**))**
Ia[27]	190.5	122.1	144.8	22.78
IIa[27]	187.9	135.4	136.6	1.2
IIb[27]	187.9	134.7	136.8	2.1
IIc[27]	187.8	133.5	136.6	3.1
IIIa[28]	182.4	131.8	137.8	6.0
IIIb[29]	182.2	130.1	137.5	7.4
IIIc[29]	182.1	128.9	137.2	3.3
IVa[27]	198.0	137.8	138.0	0.2

*Numbering refers to compounds **I**, **II**, and **IV**. **Numbering refers to compounds **III**.

Comparison of the ^{13}C NMR data of **IIa-c** with those of the respective **IIIa-c** [28,29] shows that the C=C bonds are more polar in the chromanone (**III**) derivatives. The increase in polarity results from the difference between the chemical shift of the C2(C3) atoms (Table 5). The observed changes indicate a significant resonance interaction between the substituents and the C2 carbon atoms. This was also the case with similar investigations of the analogous open-chain chalcones (**I**) and the (*E*)-2-(4-X-benzylidene)-1-benzosuberones (**IV**) [27].

Since the above parameters did not provide convincing data to explain the increased reactivity of the 4-chromanone derivatives (**III**) comparing it with the carbocyclic analogs (**II**), molecular modeling calculations were performed to compare the stereochemistry, relative energy, and molecular orbital characteristics of the transitions states of **IIa** and **IIIa** with the deprotonated form ($\mathbf{CH_3S^-}$) of the model thiol, $\mathbf{CH_3SH}$.

The electronic structure calculations revealed a clear difference in the stability of the transition states between chalcones **IIa** and **IIIa**. The presence of the oxygen atom in **IIIa** facilitates formation of hydrogen bonds between one of the electron-deficient methyl hydrogens and the polar C=C bond, resulting in a stabilized transition state. Analysis of the ring distortion reinforces this observation, where the envelope conformation of **IIIa** is more favored than the skew boat conformation of **IIa**.

The similarity in the energy gap of the frontier (HOMO and LUMO) orbitals between the TS of the two compounds (**IIa** and **IIIa**) also suggests that other factors, such as intermolecular interactions and geometric stability, are more decisive in the observed reactivities. The significant difference in Gibbs free energy barriers between **IIa** and **IIIa** indicates an easier and more efficient reaction for **IIIa.**

Additionally, the kinetic analysis reveals drastically different half-lives, with **IIIa** reacting much faster than **IIa**. These results are consistent with the lower energy barrier and higher stability of the final product in the case of **IIIa**. In conclusion, incorporation of the oxygen into the carbocyclic chalcone analogs significantly improves the stability and reactivity of the transition state and the final product. The kinetic results obtained here agree with the experimental results on the thia-Michael addition of α,β-unsaturated ketones used as fluorescent probes for imaging in single cells [30].

In the HPLC-UV chromatograms of the GSH incubations of **IIIa-c,** two separated GSH-chalcone peaks can be seen under all investigated conditions (Table 2). The ratio of the GSH-1/GSH-2 peaks (A_{GSH-1}/A_{GSH-2}) is close to unity in all pH 3.2 and pH 6.3 incubations. The ratio of the two peaks does not change over the 315-minute incubation times. However, when the incubations were performed under basic conditions (pH 8.0), the incubates showed different excesses of the least polar (GSH-2) diastereomers. The 315-minute A_{GSH-1}/A_{GSH-2} ratio of the **IIIa**, **IIIb,** and **IIIc** is 0.83, 0.50 and 0.71, respectively (Table 2). The ratios do not change over the time of incubation. It is worth mentioning that the similar reaction of the carbocyclic **IIc** resulted in formation of about twofold (2.2) excess of the more polar (GSH-1) diastereomers. The respective A_{GSH-1}/A_{GSH-2} ratios at the pH 6.3 and 3.2 incubations were 2.3 and 3.3, respectively [1].

A similar comparison of the respective NAC-incubations of **IIc** and **IIIc** showed both compounds to form only one diastereomeric peak in the pH 3.2 incubations. Under the basic (pH 8.0) conditions, the A_{NAC-1}/A_{NAC-2} ratio of **IIc** and **IIIc** was 1.58 and 0.81, respectively (Table 3). Although the stereochemistry (and the chromatographic polarity) of the adducts separated as two chromatographic peaks are not known, the different diastereomeric ratios support the above-described difference in the structure of the transition state in the two (**II** and **III**) series.

4. Materials and Methods

4.1. Chemicals and Reagents

L-glutathione and N-acetyl L-cysteine were obtained from Sigma Aldrich (Budapest, Hungary). Methanol HPLC was obtained from Honeywell (Honeywell, Hungary). Trifluoroacetic acid was obtained through VWR (Budapest, Hungary). Formic acid was obtained at Fischer Chemicals. Compounds **IIIa-c** were synthesized as previously described [10]. Their stereochemistry was verified by ^{1}H, ^{13}C NMR, and X-ray studies [29]. Purity of the samples was checked by TLC and meting point

doi:10.20944/preprints202407.1444.v1

measurement. Authentic (*E*)-**IIIa-c** were illuminated by scattered laboratory light to obtain the mixture of respective (*E*) and (Z)-isomers [31]. The structure of the (*E*)- and (*Z*)-**IIIa-c** isomers was verified by HPLC-MS (Figures S1-S8).

4.2. Preparation of Solutions

Solutions of reduced glutathione and N-acetylcysteine with different pH (pH 3.2, 6.3, and 8.0) were prepared as follows. The GSH and NAC solutions were prepared in distilled water to a total volume of 1.5 cm^3 with a concentration of 2.0 x 10 -1 $mol.L^{-1}$ (0.3 mmol GSH). The pHs were set using 1M NaOH solution. Chalcone solutions were prepared freshly before incubation to a 4.6 volume using HPLC grade methanol (4.6 cm^3 of 6.5 x 10^{-3} $mol.L^{-1}$, 0.03 mmol chalcone)

The NAC or GSH solutions were mixed with the chalcone solution to a final volume of 6.1 cm^3. The solution was then kept in the dark during preparation and analysis in a temperature-controlled (37 °C) water bath for 315 minutes. To monitor the progress of the reactions, samples were taken at time points 15, 45, 75, 105, 135, 165, 195, 225, 255, 285, and 315 minutes and analyzed by HPLC-UV. Each experimental data is the average of two parallel measurements.

4.3. RP-HPLC-UV Measurements

The measurements were performed on an Agilent 1100 HPLC system with a UV-Vis detector operating at 260 nm. The components were separated using a Zobrax Eclipse XBD-C8 (150 mm x 4.6 mm, particle size 5 µm) column (Agilent Technologies, Waldbronn, Germany). The injection volume was 10 µL. Data were recorded and evaluated using Agilent Chem Station (B.03.01). The gradient elution was performed at the flow rate of 1.2 mL/min; the mobile phase consisted of (A) water and 0.1% trifluoroacetic acid and (B) methanol and 0.1% trifluoroacetic acid. The gradient profile was as follows: an isocratic period of 8 minutes of 40% mobile phase B followed by a linear increase to 60% for 4 minutes, a second linear gradient to 90% for 3 minutes, and a 5-minute isocratic period of 90%. The column was then equilibrated to its initial conditions with a 2-minute linear gradient to 40%, followed by 3 minutes of the isocratic period.

4.4. HPLC-MS Measurements

The measurements were performed on HPLC Ultimate 3000 coupled with a mass spectrometer Q Exactive Focus (Dionex, Sunnyvale, USA). The HPLC separation was performed on an Accucore RP-MS column (150 mm x 2.1 mm, particle size 2.6 µm) using an Accucore C18 defender guard precolumn (150 mm x 2.1 mm, particle size 2.6 µm). The injection volume was 5µL; the flow rate was 0.4 mL/min. Data analysis and evaluations were performed using Thermo Scientific TranceFinder version 4.1.191.0.

A binary gradient of eluents comprised the mobile phases. (A) water and 0.1% formic acid, and (B) methanol and 0.1% formic acid. The gradient elution was as follows: 1 minute of isocratic elution of 10% of eluent B, followed by a linear increase to 95% till 14 minutes B, followed by an isocratic period of 3 minutes at 95% B, eluent B then was decreased to 10% in 0.1 minutes the column was reequilibrate at 10% eluent B for 2.9 minutes. The sampler temperature was at room temperature, and the column oven was at 40 °C. A diode array detector (DAD) was also performed at a wavelength of 260 nm, along with the MS analysis.

The Q Exactive Focus mass spectrometer was operated with an Orbitrap mass analyzer and HESI (Heated Electrospray Ionization). The mass spectrometer parameters were constant during the measurement and were set to sheat gas (nitrogen gas) 30 A.U., auxiliary gas (nitrogen gas) 10 A.U. Probe heater was set to 300 °C. Capillary temperature 350 °C The spray voltage (+) was 3500 V, and the S lens R.F. level was 50%. Mass spectrometry specifications followed the ionization method: HESI +/- having 35000 resolution at 200 m/z and a scan range of 100-1300 amu.

doi:10.20944/preprints202407.1444.v1

4.5. Molecular Modeling Analysis

Theoretical calculations were performed by DFT as implemented in the G16 software package [32]. Molecular structures were optimized using the M06-2X2 hybrid exchange and correlation functional with long-range correction, combined with the 6-311++G(d,p) basis set [33]. Frontier molecular orbital energies were calculated via DFT methods [34]. Molecular electrostatic potential maps were constructed to provide a visual representation of the electrostatic potential on the surface of a molecule, which can reveal regions of high and low electron density [35]. The electrostatic potential V(r) [35]at point r is defined as.

$$\mathrm{V}(\mathbf{r}) = \sum_{\alpha} \frac{\mathrm{Z_A}}{|\mathrm{r}_\alpha - \mathrm{r_A}|} - \int \frac{\rho(\mathrm{r})}{\mathrm{r}_\alpha - \mathrm{r}} \mathrm{dr} \tag{1}$$

where Z*a* is the charge of nuclei *a* at point **r***a* and $\rho(\boldsymbol{r})$ is the charge density at point **r**.

The local electrophilicity indices of the molecules were determined by applying the Fukui function [36,37], which can be used to predict the molecular reactive sites. The Fukui function is mathematically expressed as:

$$f(\mathbf{r}) = \left[\frac{\partial \rho(\mathbf{r})}{\partial N}\right]_v , \tag{2}$$

where N is the number of electrons in the system, and the constant term v in the partial derivative is external potential.

The electronic structure properties of the reactants (**IIa**, **IIIa,** and **CH_3S^-**), products, and transition states were calculated at the M06HF/6-31G+(d) level with the solvation model density (SMD). The SMD model has been widely used to simulate the aqueous environment in elucidating the mechanisms of organic reactions and is computationally less demanding than other continuum models [38-40].

The stationary points were characterized by analytic harmonic frequency calculations. The absence or presence of one imaginary frequency characterizes the optimized structures as local minima or transition states, respectively. The zero-point vibrational energy contributions have been considered when calculating the energy barrier.

The topological analysis [41,42] was performed in terms of electron density (ϱ), Laplacian of electron density (∇2ϱ), Lagrangian kinetic energy density [G(r)], potential energy density [V(r)] and energy density [E(r)] at the Critical Points (CP) to efficiently describe H-bonding and its concept without border. The criterion for evaluating the strength of the hydrogen bonds by topological analysis is described in [43] and references therein. The condensed Fukui indices were calculated using the atomic Hirshfeld charges obtained from the population analysis. The Multiwfn package program was used to study the topological and Fukui functions [44].

The reaction rate constant was calculated using formulations based on the thermodynamical representation of the Transition State Theory [45]

$$k(T) = \frac{k_B T}{h} e^{-\frac{\Delta G^\ddagger}{RT}} \tag{3}$$

where h is the Planck's constant, k_B is the Boltzmann constant, R is the universal gas constant, T is the absolute temperature, and $\Delta G^\ddagger$ is the activation of Gibbs free energy.

From the data of the reaction rate constant of chalcone analogs (**IIa** and **IIIa**) with the methanethiol anion obtained by (1), it is possible to calculate the half-life time using pseudo-first-order approximation [40] to the excess of methanethiol,

$$t_{1/2} = ln2 \,/(k \times [\mathrm{CH_3S^-}])$$

where $[\mathrm{CH_3S^-}]$ is the concentration of methanothiolate anion in the aqueous media.

The half-life of the reaction was studied at 298 K, and $[\mathrm{CH_3S^-}]$ in range of 10^{-2}-10^{-1} mol L^{-1}, including the experimental concentration used in this work, 4.9×10^{-2} mol L^{-1}.

5. Conclusions

This study revealed that the more cancer cell cytotoxic 3-(4-X-benzylidene)-4-chromanones (**IIIb** and **IIIc**) display an unexpectedly higher thiol-reactivity than their carbocyclic counterparts (**IIc** and **IIc**). The increased thiol reactivity was attributed to the different topography of the molecules. Using methanethiolate anion (**CH_3S^-**) as a model thiol reagent, molecular modeling results indicated that the transition state of **IIIa** is hydrogen-bond stabilized, and the adduct of **IIIa** is thermodynamically more stable than that of **IIa** (Figure 22).

Although no (Z)-isomers could be detected in the incubation mixtures, the occurrence of retro-Michael reactions can not be excluded. Taking into consideration the determining factors of the reverse process [46], formation of the resonance-stabilized methoxy-substituted derivatives can be considered as a determining factor of the higher reactivity of the methyl-substituted analogs in each series under each investigated condition (Figures 23-26 and S37, S38).

Since the cancer cell cytotoxicity of **IIIb** is much higher than that of the respective **IIb** (the ratio of the IC_{50} values is >50.0), it is reasonable to suppose that the observed difference in cytotoxicity of the two compounds is, at least in part, related to the much higher thiol reactivity of **IIIb**. On the other hand, such an increase was not observed in the analogous 4-OCH_3 (**IIc** and **IIIc**) derivatives [5]. The information gathered indicates that a further study of these compounds is warranted.

Supplementary Materials: The following supporting information can be downloaded at www.mdpi.com/xxx/: **Figure S1.** High resolution, positive mode HESI MS chromatogram of **IIIa** illuminated by scattered laboratory light. (t_r 12.52 min: (*Z*)-**IIIa**; t_r 12.82 min: **IIIa** ((*E*)-**IIIa**)). (Extracted ion chromatogram of m/z 237.0914 [(**IIIa**)+H]$^+$). **Figure S2**. High resolution, positive mode HESI MS spectrum of (*Z*)-**IIIa**. (m/z 237.0914 [(**IIIa**)+H]$^+$ and m/z 259.0733 [(**IIIa**)+Na]$^+$ t_r 12.52 min). **Figure S3**. High resolution, positive mode HESI MS spectrum of (*E*)-**IIIa**. (m/z 237.0915 [(**IIIa**)+H]$^+$ t_r 12.82 min). **Figure S4**. High resolution, positive mode HESI MS chromatogram of **IIIb** illuminated by scattered laboratory light. (t_r 13.29 min: (*Z*)-**IIIb**; t_r 13.52 min: **IIIb** ((*E*)-**IIIb**)). (Extracted ion chromatogram of m/z 251.1072 [(**IIIb**)+H]$^+$). **Figure S5**. High resolution, positive mode HESI MS spectrum of (*Z*)-**IIIb**. (m/z 251.1070 [(**IIIb**)+H]$^+$ and m/z 273.0889 [(**IIIb**)+Na]$^+$ t_r 13.28 min). **Figure S6**. High resolution, positive mode HESI MS spectrum of (*E*)-**IIIb**. (m/z 251.1072 [(**IIIb**)+H]$^+$ t_r 13.52 min). **Figure S7**. High resolution, positive mode HESI MS chromatogram of **IIIc** illuminated by scattered laboratory light. (t_r 12.72 min: (*Z*)-**IIIc**; t_r 12.84 min: **IIIc** ((*E*)-**IIIc**)). (Extracted ion chromatogram of m/z 267.1021 [(*IIIc*)+H]$^+$). **Figure S8**. High resolution, positive mode HESI MS spectrum of (*Z*)-**IIIc**. (m/z 267.1021 [(**IIIc**)+H]$^+$ and m/z 289.0840 [(**IIIc**)+Na]$^+$ t_r 12.71 min). **Figure S9**. High resolution, positive mode HESI MS spectrum of (*E*)-**IIIc**. (m/z 267.1021 [(**IIIc**)+H]$^+$ t_r 12.84 min). **Figure S10**. High resolution, positive mode HESI MS chromatograms of the **IIIa/GSH** incubate (pH 8.0 sample). **Figure S11**. High resolution, positive mode HESI MS spectrum of the **IIIa** (t_r 12.83 min) in the sample of pH 8.0 incubate, (237.0916 [(**IIIa**)+H]$^+$). **Figure S12**. High resolution, positive mode HESI MS spectrum of the **IIIa-GSH-1** conjugate (t_r 9.34 min) formed in the sample of the pH 8.0 incubate, (m/z 544.1762 [(**IIIa-GSH**)+H]$^+$). **Figure S13**. High resolution, negative mode HESI MS spectrum of the **IIIa-GSH-1** conjugate (t_r 9.34 min) formed in the sample of the pH 8.0 incubate, (m/z 542.1617 [(**IIIa-GSH**)-H]$^-$), m/z 306.0771 [**GSH**-H]$^-$) and m/z 1085.3296 [(**IIIa-GSH**)$_2$-H]$^-$). **Figure S14**. High resolution, positive mode HESI MS spectrum of the **IIIa-GSH-2** conjugate (t_r 9.47 min) formed in the sample of the pH 8.0 incubate, (m/z 544.1761 [(**IIIa-GSH**)+H]$^+$). **Figure S15**. High resolution, negative mode HESI MS spectrum of the **IIIa-GSH-2** conjugate (t_r 9.48 min) formed in the sample of the pH 8.0 incubate, (m/z 542.1617 [(**IIIa-GSH**)-H]$^-$, m/z 306.0772 [**GSH**-H]$^-$ and m/z 1085.3297 [(**IIIa-GSH**)$_2$-H]$^-$). **Figure S16**. High resolution, positive mode HESI MS chromatograms of the **IIIb/GSH** incubate (pH 8.0 sample). **Figure S17**. High resolution, positive mode HESI MS spectrum of the **IIIb** (t_r 13.52 min) in the sample of the pH 8.0 incubate, (m/z 251.1072 [(**IIIb**)+H]$^+$ and m/z 273.0891 [(**IIIb**)+Na]$^+$). **Figure S18**. High resolution, positive mode HESI MS spectrum of the **IIIb-GSH-1** conjugate (t_r 10.23 min) formed in the sample of the pH 8.0 incubate, (m/z 558.1918 [(**IIIb-GSH**)+H]$^+$). **Figure S19**. High resolution, negative mode HESI MS spectrum of the **IIIb-GSH-1** conjugate (t_r 10.23 min) formed in the sample of the pH 8.0 incubate, (m/z 556.1772 [(**IIIb-GSH**)-H]$^-$, m/z 306.0771 [**GSH**-H]$^-$ and m/z 1113.3611 [(**IIIb-GSH**)$_2$-H]$^-$). **Figure S20**. High resolution, positive mode HESI MS spectrum of the **IIIb-GSH-2** conjugate (t_r 10.37 min) formed in the sample of the pH 8.0 incubate, (m/z 558.1920 [(**IIIb-GSH**)+H]$^+$). **Figure S21**. High resolution, negative mode HESI MS spectrum of the **IIIb-GSH-2** conjugate (t_r 10.38 min) formed in the sample of the pH 8.0 incubate, (m/z 556.1772 [(**IIIb-GSH**)-H]$^-$, m/z 306.0771 [**GSH**-H]$^-$ and m/z 1113.3612 [(**IIIb-GSH**)$_2$-H]$^-$). **Figure S22.** High resolution, positive mode HESI MS chromatograms of the **IIIc-GSH** incubate (pH 8.0 sample). **Figure S23**. High resolution, positive mode HESI MS spectrum of the **IIIc** (t_r 12.85 min) in the sample of the pH 8.0 incubate, (m/z 267.1021 [(**IIIc**)+H]$^+$ and m/z 289.0840 [(**IIIc**)+Na]$^+$). **Figure S24**. High resolution, positive mode HESI MS spectrum of the **IIIc-GSH-1** conjugate (t_r 9.43 min) formed in the sample of the pH 8.0 incubate, (m/z 574.1871 [(**IIIc-GSH**)+H]$^+$). **Figure S25**. High resolution, negative mode HESI MS spectrum of the **IIIc-GSH 1** conjugate (t_r 9.44 min) formed in the sample of the pH 8.0

incubate, (m/z 572.1724 [(**IIIc-GSH**)-H]$^-$, m/z 306.0772 [**GSH**-H]$^-$ and m/z 1145.3516 [(**IIIc-GSH**)$_2$-H]$^-$). **Figure S26**. High resolution, positive mode HESI MS spectrum of the **IIIc-GSH-2** conjugate (t_r 9.61 min) formed in the sample of the pH 8.0 incubate, (m/z 574.1871 [(**IIIc-GSH**)+H]$^+$). **Figure S27**. High resolution, negative mode HESI MS spectrum of the **IIIc-GSH-2** conjugate (t_r 9.62 min) formed in the sample of the pH 8.0 incubate, (m/z 572.1724 [(**IIIc-GSH**)-H]$^-$, m/z 306.0772 [**GSH**-H]$^-$ and m/z 1145.3513 [(**IIIc-GSH**)$_2$-H]$^-$). **Figure S28**. High resolution, HESI MS chromatograms of **IIIa/NAC** incubate (pH 8.0 sample). **Figure S29**. High resolution, negative mode HESI MS spectrum of the **IIIa-NAC-1** conjugate (t_r 10.82 min) formed in the sample of the pH 8.0 incubate. (m/z 398.1072 [(**IIIa-NAC**)-H]$^-$, m/z 797.2227 [(**IIIa-NAC**)$_2$-H]$^-$, m/z 819.2043 [(**IIIa-NAC**)$_2$+Na-2H]$^-$). **Figure S30**. High resolution, negative mode HESI MS spectrum of the **IIIa-NAC-2** conjugate (t_r 10.89 min) formed in the sample of the pH 8.0 incubate. (m/z 398.1073 [(**IIIa-NAC**)-H]$^-$, m/z 797.2227 [(**IIIa-NAC**)$_2$-H]$^-$, m/z 819.2043 [(**IIIa-NAC**)$_2$+Na-2H]$^-$). **Figure S31**. High resolution, HESI MS chromatograms of **IIIb/NAC** incubate (pH 8.0 sample). **Figure S32**. High resolution, negative mode HESI MS spectrum of the **IIIb-NAC-1** conjugate (t_r 11.58 min) formed in the sample of the pH 8.0 incubate. (m/z 412.1232 [(**IIIb-NAC**)-H]$^-$, m/z 825.2541 [(**IIIb-NAC**)$_2$-H]$^-$, m/z 847.2354 [(**IIIb-NAC**)$_2$+Na-2H]$^-$). **Figure S33**. High resolution, negative mode HESI MS spectrum of the **IIIb-NAC-2** conjugate (t_r 11.70 min) formed in the sample of the pH 8.0 incubate. (m/z 412.1232 [(**IIIb-NAC**)-H]$^-$, m/z 825.2541 [(**IIIb-NAC**)$_2$-H]$^-$, m/z 847.2354 [(**IIIb-NAC**)$_2$+Na-2H]$^-$). **Figure S34**. High resolution, HESI MS chromatograms of **IIIc/NAC** incubate (pH 8.0 sample). **Figure S35**. High resolution, negative mode HESI MS spectrum of the **IIIc-NAC-1** conjugate (t_r 10.84 min) formed in the sample of the pH 8.0 incubate. (m/z 428.1179 [(**IIIc-NAC**)-H]$^-$, m/z 857.2437 [(**IIIc-NAC**)$_2$-H]$^-$, m/z 879.2251 [(**IIIc-NAC**)$_2$+Na-2H]$^-$). **Figure S36**. High resolution, negative mode HESI MS spectrum of the **IIIc-NAC-2** conjugate (t_r 10.95 min) formed in the sample of the pH 8.0 incubate. (m/z 428.1179 [(**IIIc-NAC**)-H]$^-$, m/z 857.2437 [(**IIIc-NAC**)$_2$-H]$^-$, m/z 879.2251 [(**IIIc-NAC**)$_2$+Na-2H]$^-$). **Figure S37**. Comparison of change of chromatographic peak areas of selected chalcones (**Ib**, **Ic**) and cyclic chalcone analogs (**IIb**, **IIc**; **IIb**, **IIc**; and **IVb**, **IVc**) as a function of time (min) in the chalcone/GSH incubations, pH 3.2. **Figure S38**. Comparison of change of chromatographic peak areas of selected chalcones (**Ib**, **Ic**) and cyclic chalcone analogs (**IIb**, **IIc**; **IIb**, **IIc**; and **IVb**, **IVc**) as a function of time (min) in the chalcone/NAC incubations, pH 3.2.

Author Contributions: Gábor Bognár: investigation, data curation, writing initial draft; **Fatemeh Kenari:** investigation, data curation**; Zoltán Pintér**: investigation, data curation writing initial draft, **Igor D. Borges:** investigation, data curation, writing initial draft; **Ademir J. Camargo**: investigation, data curation, writing initial review**; Heibbe C. B. Oliveira**: investigation, data curation, writing initial review**; Flávio Olimpio Sanches-Neto** investigation, data curation, writing initial review**; Valter H. Carvalho-Silva:** conceptualization, writing initial draft, writing review and editing**; Hamilton B. Napolitano:** conceptualization, writing initial draft, writing review and editing; **Pál Perjési:** project administration, conceptualization, writing initial draft, writing-review, and editing. All authors have read and agreed to the published version of the manuscript.

Funding: This study was supported by the European Union and co-financed by the European Social Fund (EFOP-3.6.1.-16-2016-00004). The financial support is highly appreciated. The authors are grateful to Conselho Nacional de Desenvolvimento Científico e Tecnológico (CNPq) and Fundação de Amparo à Pesquisa de Goiás (FAPEG). Theoretical calculations were performed in the High-Performance Computing Center of the Universidade Estadual de Goiás.

Institutional Review Board Statement: Not applicable.

Informed Consent Statement: Not applicable.

Data Availability Statement: Not applicable.

Conflicts of Interest: The authors declare no conflicts of interest.

Sample Availability: Samples of compounds **II** and **III** are available from the authors.

References

1. Part XX. Kenari, F.; Pintér, Z.; Molnár S.; Borges, I.D.; Camargo, A.J.; Napolitano, H.B.; Perjési, P. (*E*)-2-Benzylidenecyclanones: Part XIX. Reaction of (*E*)-2-(4'-X-benzylidene)-1-tetralones with cellular thiols. Comparison of thiol reactivities of open-chain chalcones and their six- and seven-membered cyclic analogs. *Int. J. Mol. Sci*. (under review).
2. Rozmer, Z.; Perjési, P. Naturally occurring chalcones and their biological activities. *Phytochem. Rev*. **2016**, *15*, 87-120.
3. Banoth, R. K.; Thatikonda, A. A review on natural chalcones an update. *Int. J. Pharm. Sci. Res*. **2020**, *11*, 546-555.
4. Constantinescu, T.; Mihis, A.G. Two important anticancer mechanisms of natural and synthetic chalcones. *Int. J. Mol. Sci*. **2022**, *23*, 11595.

5. Rajendran, G.; Bhanu, D.; Aruchamy, B.; Ramani, P.; Pandurangan, N.; Bobba, K. N. Oh, E.J.; Chung, H. Y.; Gangadaran, P.; Ahn, B.-C. Chalcone: A promising bioactive scaffold in medicinal chemistry. *Pharmaceuticals* **2022**, *15*, 1250.
6. Leite, F. F.; de Sousa, N. F.; de Oliveira, B. H. M.; Duarte, G. D.; Ferreira, M. D. L.; Scotti, M. T.; Filho, J. M. B.; Rodrigues, L. C.; de Moura, R. O.; Mendonça-Jr., F. J. B.; Scotti, L. Anticancer activity of chalcones and its derivatives: Review and in silico studies. *Molecules* **2023**, *28*, 4009.
7. Shalaby, M.A.; Rizk S.A.; Fahim, A.M. Synthesis, reactions and application of chalcones: a systematic review. *Org. Biomol. Chem*. **2023**, *21*, 5317-5346.
8. Dimmock, J.R.; Kandepu, N.M.; Nazarali, A.J.; Kowalchuk, T.P.; Motaganahalli, N.; Quail, J.W.; Mykytiuk, P.A.; Audette, G.F.; Prasad, L.; Perjési, P.; et al. Conformational and quantitative structure−activity relationship study of cytotoxic 2-arylidenebenzocycloalkanones. *J. Med. Chem*. **1999**, *42*, 1358–1366.
9. Dimmock, J.R.; Zello, G.A.; Oloo, E.O.; Quail, J.W.; Kraatz, H.-B.; Perjési, P.; Aradi, F.; Takács-Novák, K.; Allen, T.M.; Santos, C.L.; et al. Correlations between cytotoxicity and topography of some 2-arylidenebenzocycloalkanones determined by X-ray crystallography. *J. Med. Chem*. **2002**, *45*, 3103–3111.
10. Perjési, P.; Das, U.; De Clercq, E.; Balzarini, J.; Kawase, M.; Sakagami, H.; Stables, J.P.; Loránd, T.; Rozmer, Z.; Dimmock, J.R. Design, synthesis and antiproliferative activity of some 3-benzylidene-2,3-dihydro-1-benzopyran-4-ones which display selective toxicity for malignant cells. *Eur. J. Med. Chem*. **2008**, *43*, 839–845.
11. Folmer, F.; Blasius, R.; Morceau, F.; Tabudravu, J.; Dicato, M.; Jaspars, M.; Diederich, M. Inhibition of TNFα-induced activation of nuclear factor KB by Kava (*Piper Methysticum*) derivatives. *Biochem. Pharmacol*. **2006**, *71*, 1206–1218.
12. Laphanuwat, P.; Kongpetch, S.; Senggunprai, L.; Prawan, A.; Kukongviriyapan, V. Licochalcone A induces cholangiocarcinoma cell death via suppression of Nrf2 and NF-KB signaling pathways. *Asian Pac. J. Cancer Prev*. **2022**, *23*, 115–123.
13. de Freitas Silva, M.; Pruccoli, L.; Morroni, F.; Sita, G.; Seghetti, F.; Viegas, C.; Tarozzi, A. The Keap1/Nrf2-ARE pathway as a pharmacological target for chalcones. *Molecules* **2018**, *23*, 1803.
14. Egbujor, M.C.; Saha, S.; Buttari, B.; Profumo, E.; Saso, L. Activation of Nrf2 signaling pathway by natural and synthetic chalcones: A therapeutic road map for oxidative stress. *Expert Rev. Clin. Pharmacol*. **2021**, *14*, 465–480.
15. Zhuang, C.; Zhang, W.; Sheng, C.; Zhang, W.; Xing, C.; Miao, Z. Chalcone: a privileged structure in medicinal chemistry. *Chem. Rev.* **2017**, *117*, 7762-7810.
16. Gomes, M.; Muratov, E.; Pereira, M.; Peixoto, J.; Rosseto, L.; Cravo, P.; Andrade, C.; Neves, B. Chalcone derivatives: Promising starting points for drug design. *Molecules* **2017**, *22*, 1210
17. Constantinescu, T.; Mihis, A.G. Two important anticancer mechanisms of natural and synthetic chalcones. *Int. J. Mol. Sci*. **2022**, *23*, 11595.
18. Shalaby, M.A.; Rizk S.A.; Fahim, A.M. Synthesis, reactions and application of chalcones: a systematic review. *Org. Biomol. Chem*. **2023**, *21*, 5317-5346.
19. Kozurkova, M.; Tomeckova, V. Interaction of Chalcone Derivatives with Important Biomacromolecules. In *Chalcones and Their Synthetic Analogs*; Nova Science Publishers, Inc, **2020**; *Chapter 4*, 95-133.
20. Kenari, F.; Molnár, S.; Perjési, P. Reaction of chalcones with cellular thiols. The effect of the 4-substitution of chalcones and protonation state of the thiols on the addition process. Diastereoselective thiol addition. *Molecules* **2021**, *26*, 4332.
21. Aldini, G.; Altomare, A.; Baron, G.; Vistoli, G.; Carini, M.; Borsani, L.; Sergio, F. N-acetylcysteine as an antioxidant and disulphide breaking agent: The reasons why. *Free Radic. Res*. **2018**, *52*, 751–762.
22. [22].Armstrong, R. N. Structure, catalytic mechanism, and evolution of the glutathione transferases. *Chem. Res. Toxicol*. **1997**, *10*, 2-18.
23. Kupcewicz, B.; Balcerowska-Czerniak, G.; Malecka, M.; Paneth, P.; Krajewska, U.; Rozalski, M. *Bioorg. Med. Chem. Lett.* **2013**, *23*, 4102–4106.
24. Rohani, N.; Hao, L.; Alexis, M.; Joughin, B.; Krismer, K.; Moufarrej, M.; Soltis, A.; Lauffenburger, D.; Yaffe, M.B.; Burge, C.B..; Bhatia, S.N.; Gertler, F.B. Acidification of tumor at stromal boundaries drives transcriptome alterations associated with aggressive phenotypes. *Cancer Res*. **2019**, *79*, 1952–1966.
25. Kenari, F.; Molnár, S.; Borges, I.D.; Napolitano, H.B.; Perjési, P. (*E*)-2-Benzylidenecyclanones: Part XVIII. Study the possible link between glutathione reactivity and cancer cell cytotoxic effects of some cyclic chalcone analogs a comparison of the reactivity of the open-chain and the seven-membered homologs. *Int. J. Mol. Sci*. **2023**, 24, 8557.
26. LoPachin, R.M.; Gavin, T.; DeCaprio, A.; Barber, D.S. Application of the hard and soft, acids and bases (HSAB) theory to toxicant–target interactions. *Chem. Res. Toxicol*. **2012**, *25*, 239–251.
27. Perjési, P.; Linnanto, J.; Kolehmainen, E.; Ősz, E.; Virtanen E. E. *E*-2-Benzylidenebenzocycloalkanones. IV. Studies on transmission of substituent effects on ^{13}C NMR chemical shifts of *E*-2-(X-benzylidene)-1-tetralones, and -benzosuberones. Comparison with the ^{13}C NMR data of chalcones and *E*-2-(X-benzylidene)-1-indanones. *J. Mol. Struct*. **2005**, *740*, 81-89.

28. Xue-Ming, C.; Zhi-Tang, H.; Qi-Yu Z. Topochemical photodimerization of (*E*)-3-benzylidene-4-chromanone derivatives from b-type structures directed by halogen groups. *Tetrahedron* **2011**, *67*, 9093e9098.
29. Valkonen, A.; Laihia, K.; Kolehmainen, E.; Kauppinen, R.; Perjési, P. Structural studies of seven homoisoflavonoids, six thiohomoisoflavonoids, and four structurally related compounds. *Struct. Chem*. DOI: 10.1007/s11224-011-9860-6.
30. Chen, J.; Jiang, X.; Carroll, S. L.; Huang, J.; Wang, J. Theoretical and experimental investigation of thermodynamics and kinetics of thiol-Michael addition reactions: A case study of reversible fluorescent probes for glutathione imaging in single cells. *Org. Letters*, **2015**, *17*, 5978–5981.
31. Kupcewicz, B.; Balcerowska-Czerniak, G.; Malecka, M.; Paneth, P.; Krajewska, U.; Rozalski, M. *Bioorg. Med. Chem. Lett*. **2013**, *23*, 4102–4106.
32. Frisch, M.; Trucks, G.; Schlegel, H.; Scuseria, G.; Robb, M.; Cheeseman, J.; Scalmani, G.; Barone, V.; Petersson, G.; Nakatsuji, H. Gaussian 16 Revision C. 01. 2016; Gaussian Inc. *Wallingford CT* **2016**, *421*.
33. Zhao, Y.; Truhlar, D.G. The M06 suite of density functionals for main group thermochemistry, thermochemical kinetics, non-covalent **interactions**, excited states, and transition elements: Two new functionals and systematic testing of four M06-class functionals and 12 other functionals. *Theor. Chem. Acc.* **2008**, *120*, 215–241.
34. Zhang, G.; Musgrave, C.B. Comparison of DFT methods for molecular orbital eigenvalue calculations. *J. Phys. Chem. A.* **2007**, *111*, 1554–1562.
35. Weiner, P.K.; Langridge, R.; Blaney, J.M.; Schaefer, R.; Kollman, P.A. Electrostatic potential molecular surfaces. *Proc. Natl. Acad. Sci. U.S.A.* **1982**, *79*, 3754–3758.
36. Náray-Szabó, G.; Ferenczy, G.G. Molecular electrostatics. *Chem. Rev.* **1995**, *95*, 829–847.
37. Fukui, K. The role of frontier orbitals in chemical reactions (Nobel Lecture). *Angew. Chem. Int. Ed. Engl.* **1982**, *21*, 801–809.
38. Fukui, K. Role of frontier orbitals in chemical reactions. *Science* **1982**, *218*, 747–754.
39. Sanches-Neto, F.; Coutinho, N.; Aquilanti, V.; Silva, W.; Carvalho-Silva, V. Mechanism and kinetics of the degradation of nitazoxanide and hydroxychloroquine drugs by hydroxyl radicals: theoretical approach to ecotoxicity. *J. Braz. Chem. Soc*. **2023**, *34*, 1119-1129.
40. Sanches-Neto, F.O.; Coutinho, N.D.; Palazzetti, F.; Carvalho-Silva, V.H. Temperature dependence of rate constants for the H(D) + CH_4 reaction in gas and aqueous phase: Deformed transition-state theory study including quantum tunneling and diffusion effects. *Struct. Chem.*, **2020**, *31*, 609–617.
41. Sanches-Neto, F.O.; Ramos, B.; Lastre-Acosta, A.M.; Teixeira, A.C.S.C.; Carvalho-Silva, V.H. Aqueous picloram degradation by hydroxyl radicals: Unveiling mechanism, kinetics, and ecotoxicity through experimental and theoretical approaches. *Chemosphere*, **2021**, *278*, 130401.
42. Bader, R.F.W. Atoms in molecules. *Acc. Chem. Res*. **1985**, *18*, 9–15.
43. Matta, C.F.; Boyd, R. J. (2007). The Quantum Theory of Atoms in Molecules: From Solid State to DNA and Drug Design (C. F. Matta and R. J. Boyd, Eds.). John Wiley & Sons. 2007.
44. de Almeida, L.R.; Carvalho, Jr., P.S.; Napolitano, H.B.; Oliveira, S.S.; Camargo, A.J.; Figueredo, A.S.; de Aquino, G.L.B.; Carvalho-Silva, V.H. Contribution of directional dihydrogen interactions in the supramolecular assembly of single crystals: Quantum chemical and structural investigation of $C_{17}H_{17}N_3O_2$ azine. *Cryst. Growth Des.* **2017**, *17*, 10, 5145–5153.
45. Lu, T.; Chen, F. Multiwfn: A multifunctional wavefunction analyzer. *J. Comput. Chem.* **2012**, *33*, 580–592.
46. Laidler, K.J.; Eyring, H.; Glasstone, S.; Laidler, K.J.; Eyring, H. *The Theory of Rate Processes: The Kinetics of Chemical Reactions, Viscosity, Diffusion and Electrochemical Phenomena* (Inc. McGraw-Hill Book Company, Ed.). McGraw-Hill. 1941.